MAX-PLANCK-INSTITUT FÜR PLASMAPHYSIK

GARCHING BEI MÜNCHEN

EVOLUTION OF HIGH-DENSITY PARTICLE CLOUDS IN MAGNETICALLY CONFINED PLASMAS

Gerardo Zavala Guzmán

IPP 5/33 December 1989

A dissertation submitted in partial fulfillment
of the requirements for the degree of
Doctor of Philosophy
(Nuclear Engineering Department)
in the University of Michigan
December 1989

MAX-PLANCK-INSTITUT FÜR PLASMAPHYSIK

GARCHING BEI MÜNCHEN

EVOLUTION OF HIGH-DENSITY PARTICLE CLOUDS IN MAGNETICALLY CONFINED PLASMAS

Gerardo Zavala Guzmán

IPP 5/33 December 1989

A dissertation submitted in partial fulfillment
of the requirements for the degree of
Doctor of Philosophy
(Nuclear Engineering Department)
in the University of Michigan
December 1989

Evolution of High-Density Particle Clouds in Magnetically Confined Plasmas

ABSTRACT

The subject of this study is the spatial and time evolution of initially low-temperature high-density particle clouds in magnetically confined hot plasmas, such as those produced by ablating cryogenic hydrogen pellets in fusion machines. Particular attention is given to such physical processes as heating of the cloud by the energy fluxes carried by incident plasma particles (classical flux-limited energy transport by thermal electrons along the magnetic field lines, anomalous heat conduction across them), gasdynamic expansion with $\vec{j} \times \vec{B}$-produced deceleration in the transverse direction, finite-rate ionization and recombination (collisional and radiative) processes, and magnetic field convection and diffusion.

The Lagrangian approximation used allows one to take into account all relevant physical processes that affect the radial expansion and deceleration of the cloud particles, including the change of the magnetic field topology.

The results show the existence of a distinct structure in the ablatant cloud surrounding an ablating pellet: a hollow temperature profile coupled to a peaked density profile in the plane normal to the magnetic field direction. The lifetime of this structure is measured on hydrodynamic time scales. The basic properties of the cloud, such as its radial extent, average temperature, bulk density, etc., are complex functions of the pellet ablation rate, the parameters of the background plasma, and the magnetic field strength applied. Simple analytical or ad hoc description of this functionality, as done in present ablation models, does not seem to be possible.

ACKNOWLEDGMENTS

The author would like to thank his supervisor, Professor Terry Kammash, for proposing the topic of this PhD thesis and for maintaining a keen interest in its progress.

He is particularly grateful to Dr. Lajos Lengyel, whose constant encouragement, invaluable advice, and helpful guidance greatly contributed to the completion of the study.

Professor Karl Lackner is thanked for his constructive criticism and support.

Thanks are also due to Dr. Wolfgang Schneider and Dr. Josef Neuhauser for many useful discussions, suggestions, and contributions.

Finally, the author wishes to express his sincere appreciation to IPP and the Max Planck Society for awarding him a doctoral fellowship for the duration of the work.

I. INTRODUCTION

An essential problem attracting growing attention in current fusion-oriented plasma physics research is how to replenish particles lost from the plasma volume. The same problem is expected to appear, in a more demanding form, in future magnetic confinement fusion reactors operated with hydrogen isotope plasmas. In such reactors, the reaction product - helium ash in the given case - must be continuously removed and replaced, just as the fraction of unburned fuel particles that inevitably leaves the reaction volume with the helium particles. Under steady-state conditions, the outward-directed particle fluxes have to be compensated by an equivalent stream of neutral particles supplied to the plasma by external sources. There are two basic methods currently in use for introducing fresh particles into the plasma volume: gas blow-in (gas puffing) and injection of cryogenic hydrogen isotope pellets into the plasma [1, 2]. A further method by which particles are supplied to the plasma from exterior sources is the injection of high-energy neutral particle beams into the plasma, primarily for the purpose of increasing the global plasma energy (the neutral particles are slowed down and ionized by collisions with the plasma particles, their kinetic energy thus being converted into thermal plasma energy). In this case, the particle beam has a much smaller effect on the global particle balance than on the energy balance. Nevertheless, neutral beam injection is being considered as an auxiliary means of particle fueling in some future tokamak reactor scenarios.

Gas blow-in, which is the simplest fueling method, and which is currently being used in all operational tokamaks, supplies particles to just the outer plasma regions . The relatively low-energy gas stream interacting with the hot plasma particles already becomes ionized (and confined to magnetic flux surfaces) in the plasma boundary layer.

However, the results of numerous experimental and theoretical investigations show that the performance characteristics of present and future tokamaks may be substantially increased by supplying a sufficiently large number of fresh fuel particles direct to the plasma core (see, for example, Alcator-C [3], JET [4], ASDEX [5], TFTR [6], and D-III [7], and see Ref. [8] for predictive scenarios). In particular, the production of centrally peaked density profiles in tokamak plasmas was found to substantially reduce particle and energy transport in the central plasma region and thus improve the global confinement properties. Also the density and beta limits observed in pellet-fueled tokamaks were found to be higher than those in gas-fueled machines. The MHD and sawtooth activities can be notably affected (e.g. suppressed in some cases) by pellet injection. A

detailed review of the state of the art of pellet injection and associated toroidal confinement phenomena is given in Ref. [9]. The realization of special scenarios in future devices by means of deep pellet injection, such as density ramp-up and achievement of ignition, seems to be promising [8]. On the other hand, continuous fueling of tokamak reactors may not necessarily require deep fueling [10]. Nevertheless, the possible advantages of fueling fusion machines by means of pellet injection has initiated lively investigation, both theoretical and experimental, in this field.

The basic process that determines the effectiveness of pellet fueling, i.e. the lifetime and penetration depth of cryogenic pellets in hot plasmas, is the pellet erosion or ablation process. This process involves the interaction of the ambient plasma particles with the pellet surface (particle slow-down and energy deposition phenomena). There have been a number of physical models proposed for describing the pellet ablation process, the best known being the so-called neutral gas shielding ablation model (see Refs. [11, 12, and 13]). This model is based on a one-dimensional spherically symmetric solution of the corresponding hydrodynamic equations. The energy transfer from the undisturbed plasma (the analysis is restricted to thermal electrons as energy carriers) to the cloud surrounding the pellet is calculated by means of stopping length calculations taking elastic and inelastic collisions into account. The violation of the condition of spherical symmetry by the presence of the magnetic field was neglected in these analyses. The effect of the magnetic confinement of the ionized ablatant was estimated in Ref. [14], in which the dynamics of a one-dimensional channel flow with a mass source active at the inlet section of the channel was considered. The strength of the mass source, i.e. the ablation rate, was calculated as a function of the (local) plasma parameters at the channel inlet by means of the Parks-Turnbull formula [13] ("plasma shielding"). The results of this analysis showed the significant effect of the magnetic confinement of the shielding cloud on the ablation rate and thus warranted increased attention to this problem. The neutral gas shielding model was subsequently revised [15] by assuming an ad hoc ionization radius for the ablatant, and that the ionized pellet particles pile up in a channel whose cross-section is defined by this ionization radius. The detailed characteristics of the shielding cloud surrounding the pellet are not considered in this work.

The first estimate of the cloud characteristics was given in Ref. [16] on the basis of zero-dimensional conservation equations (particle, momentum, and energy) by taking finite-rate ionization and magnetic confinement into account. Cloud temperatures and densities of the order of 1 to 3 eV and $\approx 10 \times^{24} m^{-3}$ were predicted by this analysis. An attempt was made by Parks [17] to obtain quantitative estimates of the magnitude of the interaction between the ablatant

and the magnetic field. He calculated the magnetic interaction parameter of a conducting and spherically expanding fluid in a magnetic field by taking the velocity distribution from the neutral gas shielding ablation model (zero magnetic field effects). He concluded that the magnetic field effect is not essential. The problem of magnetic shielding was also addressed by Kuteev [18], and by Zavala and Kammash [19].

The question of ablatant expansion and interaction of this high-density partially ionized substance with the magnetic field was recently re-addressed by means of a self-consistent 1-D MHD model [20]. The cloud parameters computed in [20b] are in good agreement with measured data reported for PLT [21], TFR [22], TEXT [23], and TFTR [24].

II. PROBLEM DEFINITION AND QUALITATIVE DESCRIPTION OF THE PHYSICAL PROCESS

The objective of the present work is to help to clarify a relevant detail of the rather complex physical process of pellet-plasma interaction: the time evolution of the high-density cloud released by the eroding (ablating) pellet in a magnetically confined plasma. The cloud enveloping the pellet may be dense enough to intercept the energetic plasma particles and may thus shield the pellet and prolong its lifetime. Furthermore, as will be seen, a pellet injected into a tokamak plasma traverses its own cloud. Hence, from the point of view of the ablation dynamics, the temperature and density distributions, e.g. "structures", evolving in front of the pellet are of great interest. In a recent work, R.D. Durst [25; see also 23] experimentally investigated the evolution of the ablatant cloud surrounding the pellet. Durst's results show that pellet shielding cannot be viewed as a quasi-equilibrium process: oscillations in the ablation rate are most likely due to oscillations in the pellet shielding, i.e. due to the "structures" evolving in the shielding cloud. Realistic predictions concerning pellet lifetimes, penetration depths, and the required injection velocities for fusion-grade plasmas call for a thorough understanding of the details of those physical processes that determine or substantially affect the lifetime of pellets in hot plasmas. The evolution of the shielding cloud surrounding the pellet is one of these details.

Let us now briefly describe what is believed to happen when a pellet is injected into a plasma. A cryogenic hydrogen isotope pellet ($T \leq 10^o K$, $n_{H_2} \approx 2.7 \times 10^{28}\ m^{-3}$, $n_{D_2} \approx 3.1 \times 10^{28}\ m^{-3}$, $n_{T_2} \approx 3.2 \times 10^{28}\ m^{-3}$) exposed to a hot plasma is heated primarily by the plasma particles, both thermal and non-thermal, incident on the pellet surface. Radiation is believed to affect the pellet

much less than the energy fluxes carried by the incident particles. The pellet heating may thus be a surface phenomenon (the stopping length of hydrogen plasma particles of thermal temperatures $T_e \approx T_i \lesssim 20$ keV in frozen H_2 or D_2 pellets amounts to a few μm [26]), or, in the case of high-energy non-thermal particles (such as runaway electrons with E_e in the MeV range), a volume process. In this second case, pellet heating is usually manifested in explosion-like mass disintegration. If there is a cloud surrounding the pellet, the energy carriers originating from the undisturbed plasma may be partially or totally intercepted by the cloud, and the pellet "sees" just the cloud layers adjacent to its surface.

As has been mentioned, the questions of pellet heating, pellet erosion and pellet disintegration are not considered in the present work. The analysis is limited to the evolution of the cloud formed around the pellet by the ablated pellet particles. The pellet itself is be replaced in our model by a mass source (particle source) of given strength.

The low-temperature high-density cloud enveloping the pellet is heated by the incident plasma particles. In the absence of non-thermal particles, the energy flux carried by the electrons dominates over the flux carried by the ions. As the temperature and the pressure of the cloud increase, the cloud starts to expand: this expansion remains unaffected by the magnetic field (i.e. remains spherically symmetric) as long as the particles remain neutral. During this initial expansion phase, the energy transfer to the cloud increases proportionally to the cloud surface exposed to the plasma.

At some time instant, the cloud particles begin to become ionized and to interact with the magnetic field, i.e. their radial expansion becomes decelerated and eventually comes to a full stop. Initial investigations based on a single Lagrangian cell approximation [20] showed that a bulk ionization degree of a few per cent is sufficient to trigger a full stop of the transverse expansion (e.g. of the expansion in the direction perpendicular to the magnetic field direction). For plasma parameter ranges and particle deposition rates (e.g. ablation rates) of current interest, the stopping radii vary in the mm range (up to a few cm for reactor-grade plasma parameters). The associated stoppping times are in the μs range. The expanding partially or fully ionized cloud - referred to hereafter as "plasmoid" - distorts the magnetic field: a transient magnetic cavity may form inside the cloud.

In the case of pellets in tokamak plasmas, the radial deceleration and the stopping of the transverse expansion may be followed by a few overdamped compressive oscillations with a characteristic frequency that is defined by the respective Alfvén time: $f^{-1} \approx \tau^A = R_{max}/v_A$, where R_{max} is the maximum

cloud radius attained and v_A is the Alfvén velocity based on the cloud density and the applied magnetic field strength [20]. The cause of these oscillations is the periodic interchange of the energies stored in the (displaced) magnetic field and in the plasmoid (primarily kinetic energy). While the dynamic processes associated with the ionization and radial confinement processes are characterized by the relatively short Alfvén time scale (μs range), the subsequent phase of axial expansion is associated with a notably larger hydrodynamic time scale defined by the heat input and gasdynamic expansion rates. The rediffusion of the magnetic field into the ionized cloud occurs on the resistive diffusion time scale, which is of the same order of magnitude as, or larger than, the hydrodynamic time scale (ms range). Because of this relatively slow time variation, this second phase that follows the radial deceleration process shall be referred to as the "quasi-steady" or "quasi-equilibrium" phase. During this phase, the plasmoid is "funneled" into a magnetic flux tube whose radius is given by the plasmoid radius prevailing at the end of the Alfvén oscillations.

The model presented in Ref. [20] was validated with the help of the results of magnetospheric barium release experiments [27] in which the observed stopping radii were in the km range, whereas the associated stopping times and m.f. rediffusion times were measured in minutes to hours. Satisfactory agreement between the measured data and calculated results was found.

It is of interest to see how far the conclusions obtained in the single-cell Lagrangian approximation of [20] become modified in the multi-cell approximation used in this work. The major difference between the two approximations is the allowance made for spatially nonuniform ionization (owing to the direct contact between the hot plasma and the outermost Lagrangian cell) and the resulting ionization wave propagating toward the plasmoid center (symmetry axis). The radial variations of the ionization state, Lorentz force, magnetic field pressure, etc. accounted for in the present work, may modify the initial oscillatory Alfvén transition phase and the "quasi-steady" or "quasi-equilibrium" plasmoid properties resulting after completion of the radial confinement process.

Besides its obvious academic interest, the question of radial structures in ablatant clouds has an essential practical application: A pellet injected into a plasma in a direction perpendicular to the magnetic field with a velocity much lower than the cloud expansion velocity (as will be seen, typically in the ratio $\approx 1/10$) traverses its own shielding cloud. As Durst's study [25, 23] shows, any structures in the medium located ahead of the pellet may affect the local ablation and thus particle deposition rates, the pellet lifetime, and the attainable penetration depths. It is the aim of the present work to obtain quantitative information on the variation of the plasmoid state parameters across the shiel-

ding cloud surrounding a stationary or slowly moving mass source (e.g. ablating pellet).

III. MATHEMATICAL MODEL

(a) Model Description

For the sake of numerical convenience, the expanding and partially ionized particle cloud is subdivided into a discrete number of nested annular volume elements, each annulus representing a Lagrangian cell. The uniform magnetic field applied is assumed to be parallel to the axis of the annulus (see Fig. 1a): $\vec{B} = \hat{z}B(r,t)$. The applied magnetic field is spatially uniform: $\vec{B}(t=0) = \text{const} = \hat{z}B_o$. Since the energy flux affecting the cloud from the side of the plasma particles is assumed to be identical in the $+\hat{z}$ and $-\hat{z}$ directions, the $z = 0$ plane is assumed to be a symmetry plane and only the $0 \leq z$ domain shall be considered (i.e. half of the total cloud mass). The initial cloud geometry is given in the form of a regular cylinder $z(k) = \text{const} = z_o, 0 \leq r(\ell) \leq r_p$, where k is the index of a cell (of intrinsic cell properties or cell length) and ℓ is the index of a cell boundary; $r_p = r_{src}$ represents a fictitious source (pellet) radius.

For times $0 \leq t \leq \tau_{src}$ the mass source is turned on, and all Lagrangian cells with inner radii not exceeding the source radius $r_p = r_{src} = \text{const} = R_{cld}(t=0)$ are supplied with cold neutral particles at a rate proportional to their area-coverage ratio: $\dot{N}_{src}(k) = \dot{N}_{src} \cdot a_\perp(k)/A_{\perp src}$, where $\dot{N}_{src}$ is the total mass source strength (equivalent pellet ablation rate), $a_\perp(k)$ is the end surface of the Lagrangian cell covered by (i.e. within the limits of) the source radius, and $A_{\perp src} = \pi r_p^2$ is the total lateral surface of the particle-emitting region. When, in the course of radial expansion, the inner radius of an annular cell becomes larger than r_{src}, the number of particles supplied to this cell is cut to zero. Since in realistic physical scenarios the incident plasma particles primarily affect the lateral (i.e. end) surfaces of a pellet, these surfaces seem to be subject to enhanced erosion. Hence the definition of the source geometry used in this work, i.e. the limitation of the mass source region to the original pellet size, appears to be an acceptable approximation. It is assumed that the nested cylindrical annuli retain their initial geometry during the entire cloud expansion, i.e. their boundaries remain nested straight and concentric cylinders. This means, from a mathematical point of view, that the dynamics of the radial expansion is decoupled from that of the axial motion (although, as can be seen from the energy equation, the flow work term used in the calculation of the pressure and/or temperature of a Lagrangian cell accounts for both the radial and the

axial motions). Since the primary objective of the present work is to obtain information on the radial structures in ionizing particle clouds expanding in magnetic fields, calculating the axial flow dynamics has the primary purpose of correcting the radial distributions for the effects of axial expansion, and, at the same time, of obtaining information on the rate of cloud expansion in the axial direction (length of the structures, etc) as well.

Within a Lagrangian cell, the plasmoid properties are assumed to be uniform, i.e. the variation of the plasmoid state properties along the magnetic field lines is neglected: $\partial/\partial z \equiv 0$. The longitudinal nonuniformities associated with the finite stopping lengths of the incident plasma particles moving along the magnetic field lines are neglected in this approximation: it is assumed that the energy transported by these particles is distributed instantaneously and uniformly along each plasmoid cell. The axial variation is also neglected in the calculation of the magnetic field convection and diffusion processes (infinitely long cylindrical plasmoid approximation). The magnitude of the end effects associated with the finite length of the plasmoid in the z direction was estimated in Ref. [20a]; it was found to be insignificant in most cases of practical interest.

The heat fluxes affecting the cloud in the axial and transverse directions are calculated differently: the axial heat flux is defined in terms of the energy flux carried by the thermal electrons along the magnetic field lines, whereas the heat flux in the direction perpendicular to the magnetic field is assumed to be a conductive heat flux defined in terms of the electron thermal conduction across the magnetic field lines. For the first case, a flux-limiting factor of $f_{e_\parallel} = 0.5$ has been assumed, i.e. $q_\parallel = f_{e_\parallel}(\frac{1}{4} n_e v_{e_{th}} E_e)$. Computations performed with this value yielded rather good correspondence with experimentally observed properties [20b]. The value of the transverse electron conductivity $\chi_{e_\perp}$ was deduced from experiments aimed at measurement of the heat pulse propagation speeds in tokamak plasmas. Such pulses were produced by, for example, injecting pellets into the plasma [28]. In accordance with Gondhalekar [28], $\chi_{e_\perp} \approx 1 \quad m^2/s$ has been used in the present calculations. Admittedly, the combination of the values of $f_{e_\parallel}$ and $\chi_{e_\perp}$ is, to a certain extent, arbitrary; relaible selection of these constant factors should require series of experiments aimed at the determination of these quantities.

(b) Basic Equations

In the present work, a single-velocity, single-temperature, three-species fluid approximation is used in which the number densities of the species (neutrals, ions, and electrons) are related and defined by means of finite ionization and recombination rates. Allowance is made for the interaction of the conducting cloud with the magnetic field and for the distortion of the applied magnetic

field by the expanding plasmoid.

The basic set of magnetohydrodynamic conservation equations used is as follows (the MKS/ISU system of units is used throughout this work):

heavy-particle conservation:

$$\frac{\partial n_h}{\partial t} + \nabla \cdot (n_h \vec{v}) = \dot{n}_s \ , \tag{b.1}$$

where $n_h = n_a + n_i$; electron conservation:

$$\frac{\partial n_e}{\partial t} + \nabla \cdot (n_e \vec{v}) = \dot{n}_e \ , \tag{b.2}$$

momentum conservation:

$$\rho \frac{\partial \vec{v}}{\partial t} + \rho(\vec{v} \cdot \nabla)\vec{v} = -\nabla(p + q_v) + \vec{j} \times \vec{B} + m_s \dot{n}_s (\vec{v}_s - \vec{v}) \ , \tag{b.3}$$

conservation of total energy:

$$\begin{aligned} \frac{\partial}{\partial t}(\frac{1}{2}\rho v^2 + \frac{p}{\gamma - 1} + \frac{B^2}{2\mu_o}) + \nabla \cdot [(\frac{1}{2}\rho v^2 + \frac{p}{\gamma - 1})\vec{v}] = \\ \dot{q}_{int} - \nabla \cdot \vec{q} - \nabla \cdot (\vec{E} \times \frac{\vec{B}}{\mu_o}) + (\frac{kT_s}{\gamma - 1} + \frac{1}{2} m_s v_s^2)\dot{n}_s. \end{aligned} \tag{b.4}$$

These equations are supplemented by
Maxwell's equations:

$$\nabla \times \vec{B} = \mu_o \vec{j}, \tag{b.5}$$

$$\nabla \times \vec{E} = -\frac{\partial \vec{B}}{\partial t}, \tag{b.6}$$

$$\nabla \cdot \vec{B} = 0; \tag{b.7}$$

Ohm's law:

$$\vec{j} = \sigma(\vec{E} + \vec{v} \times \vec{B}), \tag{b.8}$$

a magnetic field diffusion equation (that follows from Maxwell's equations):

$$\frac{\partial \vec{B}}{\partial t} = \nabla \times (\vec{v} \times \vec{B}) + \nabla \cdot (\chi_m \nabla \vec{B}) \ , \tag{b.9}$$

and an equation of state:

$$p_k = (nkT)_k, \qquad k = e, i, a, s \tag{b.10}$$

$$\begin{aligned} p &= (n_e + n_i + n_a)kT \\ &= (1 + \alpha) n_h kT. \end{aligned} \tag{b.11}$$

In the above equations, subscripts e, i, a, h, and s denote, respectively, electrons, ions, neutrals, heavy particles, and particles supplied by the mass source. In the single-velocity approximation used, the momentum conservation equation (b.3) represents the sum of the momentum balance equations written for the components a, e, and i, respectively. The quantity q_v appearing in this equation represents artificial viscosity. The mass source strength $\dot{n}_s$ is assumed to be given, whereas $\dot{n}_e$, as will be seen, is calculated on the basis of the plasmoid properties. The cloud density ρ is given by $\rho = n_a m_a + n_i m_i + n_e m_e \simeq n_h m_a$, where m_a is the mass of the neutral atoms considered. Since the present calculations are limited to deuterium, and only dissociative ionization is taken into account, it follows that $D_2 \rightarrow 2D^+ + 2n_e$, and $n_i = n_e$.

The term $\dot{q}_{int}$ appearing in the total energy equation represents internal energy sources: it shall be replaced in our case by a term representing the power per unit volume expended on ionization: $\dot{q}_{int} = -\epsilon_i \dot{n}_e$, ϵ_i being the energy spent on ionization (plus dissociation) of an atom. The second and third terms on the R.H.S. of the total energy equation are the divergences of the heat flux vector and of the Poynting vector, respectively. The magnetic field diffusion coefficient χ_m appearing in eq. (b.9) is defined by the local value of the electrical conductivity:

$$\chi_m = (\mu_o \sigma)^{-1} \ , \tag{b.12}$$

whereas in the calculation of σ both electron-neutral and electron-ion collisions are taken into account:

$$\sigma = \frac{n_e e^2}{m_e \nu_e} \ , \tag{b.13}$$

$$\nu_e = \nu_{ea} + \nu_{ei} \ . \tag{b.14}$$

The ionization rate equation is of the form

$$\dot{n}_e = n_e n_a \alpha_c - n_e^2 n_i \beta_c + n_a \alpha_\nu - n_e n_i \beta_\nu \ , \tag{b.15}$$

where α and β denote the ionization and the recombination rates, and the subscripts c and ν collisional and radiative processes, respectively. Detailed equilibrium is assumed, i.e. with $\dot{n}_e \equiv 0$ one has

$$n_e n_a \alpha_c)_{eql} = n_e^2 n_i \beta_c)_{eql} \qquad \text{and} \qquad n_a \alpha_\nu)_{eql} = n_e n_i \beta_\nu)_{eql} \ ,$$

and because of the high collisionality, the equilibrium electron (ion) density is defined in terms of the Saha equation:

$$n^2_{e_{eql}} = n^2_{es} = n_a \left(\frac{2\pi m_e k T_e}{\hbar^2} \right) exp\left(-\frac{\epsilon_i}{k T_e}\right) \ , \tag{b.16}$$

where $k = 1.38 \times 10^{-23} J/K$ is the Boltzmann constant and $\hbar = 6.625 \times 10^{-34} Js$ is the Planck constant, respectively. In the present work, an effective ionization energy $\epsilon_i \simeq 30\ eV$ is assumed (with allowance for the radiative energy losses associated with the successive excitation and de-excitation processes proceeding a single ionization event), although the dissociation and ionization energies of the hydrogen species considered are 2.24 eV and 13.6 eV, respectively. Hence, taking advantage of the condition of detailed equilibrium, the ionization rate equation reduces to

$$\dot{n}_e = (\beta_{3b} n_e + \beta_\nu)(n_{es}^2 - n_e^2), \qquad (b.17)$$

where $\beta_{3b} = \beta_c$ is the three-body recombination coefficient [29], and β_ν is taken from Ref. [30]. The collision frequencies ν_{ea} and ν_{ei} are taken from Refs. [17] and [31], respectively.

A conservation equation can be obtained for the kinetic energy by dot-multiplying eq. (b.3) by the velocity vector $\vec{v}$ (the $\vec{j} \times \vec{B}$ term is expressed by means of the gradient of the magnetic pressure $p_m = B^2/2\mu_o$):

$$\begin{aligned} \frac{\partial}{\partial t}(\frac{1}{2}\rho v^2) + \nabla \cdot [(\frac{1}{2}\rho v^2)\vec{v}] = &- \nabla \cdot [(p + p_m + q_v)\vec{v}] \\ &+ (p + p_m + q_v)\nabla \cdot \vec{v} \\ &+ \frac{1}{2} m_s (2\vec{v}_s - \vec{v}) \cdot \vec{v} \dot{n}_s . \end{aligned} \qquad (b.18)$$

Furthermore, a conservation equation is obtained for the magnetic energy per unit volume (= magnetic pressure) by rewriting eq. (b.9) in the form

$$\frac{\partial \vec{B}}{\partial t} = (\vec{B}\nabla)\vec{v} - \vec{B}(\nabla \cdot \vec{v}) - (\vec{v}\nabla)\vec{B} + \nabla(\chi_m \nabla \vec{B})$$

and multiplying it by the vector $\vec{B}/\mu_o$ (χ_m = const, $\vec{B} = \hat{z}B$, and $\partial/\partial z \equiv 0$ are assumed):

$$\frac{\partial}{\partial t}(p_m) + \nabla \cdot (p_m \vec{v}) = \nabla \cdot (\chi_m \nabla p_m) - p_m \nabla \cdot \vec{v} - \frac{\chi_m}{\mu_o}(\nabla B)^2 . \qquad (b.19)$$

Under the same conditions, the equivalent expression obtained for the magnetic field can be written as

$$\frac{\partial}{\partial t} B + \nabla \cdot (B\vec{v}) = \nabla \cdot (\chi_m \nabla B) . \qquad (b.20)$$

The first term of the R.H.S. of eq. (b.19) corresponds to the magnetic field energy flux conducted through the boundary enveloping the plasmoid and the second to volumetric changes (i.e. to the magnetic pressure work). The third

term is proportional to the square of the magnetic field gradient and, within the plasmoid volume considered, is small in relation to the other terms in most cases of practical interest.

By subtracting the kinetic and magnetic energy constituents from the total energy, one obtains an equation for the internal energy conservation:

$$\frac{\partial}{\partial t}\left(\frac{p}{\gamma-1}\right)+\nabla\cdot\left(\frac{p\vec{v}}{\gamma-1}\right)=-\nabla\cdot\vec{q}-\epsilon_i\dot{n}_e-(p+q_v)\nabla\cdot\vec{v} + \left[\frac{kT_s}{\gamma-1}+m_s(v_s-s)^2\right]\dot{n}_s. \tag{b.21}$$

(c) Lagrangian Representation

We now integrate the various conservative properties of the cloud, such as the particle numbers, momentum components, internal and magnetic energies, etc, over the volumes of the individual Lagrangian cells by recalling that the plasmoid parameters are assumed to be constant over each cell volume and no particle crosses the cell boundaries. In the integrals that follow, advantage will be taken of Gauss's divergence theorem

$$\int_V(\nabla\cdot\vec{G})dV=\int_S\vec{G}\cdot d\vec{\sigma} \tag{c.1}$$

and Leibnitz's rule

$$\frac{d}{dt}\int_V g dV=\int_V\left(\frac{\partial g}{\partial t}\right)dV+\int_S g\vec{v}\cdot d\vec{\sigma}\ . \tag{c.2}$$

In these expressions, $d\vec{\sigma}=\hat{n}d\sigma$ and dV denote the surface and volume differentials associated with the surface S and the volume V of the control volume considered, and $\hat{n}$ is the outward-directed normal.

Let us now take an arbitrary intrinsic plasmoid state parameter f which, just as any other plasmoid parameter, is assumed to be constant over the plasmoid cell volume V and to satisfy the conservation equation

$$\frac{\partial f}{\partial t}+\nabla\cdot(f\vec{v})=\dot{f}_s+g\ . \tag{c.3}$$

The integral of this equation over the plasmoid cell volume yields

$$\int_V\left(\frac{\partial f}{\partial t}\right)dV+\int_V\nabla\cdot(f\vec{v})dV=\frac{d}{dt}\int_V f dV-\int_S f\vec{v}\cdot d\vec{\sigma}+\int_S f\vec{v}\cdot d\vec{\sigma} - \int_V\dot{f}_s dV+\int_V g dV\quad , \tag{c.4}$$

i.e.

$$\frac{d}{dt}(F) = \dot{F}_s + G \ , \tag{c.5}$$

where the quantities F, $\dot{F}_s$, G, owing to their constancy over the plasmoid cell volume, are

$$F = \int_V f dV = fV, \qquad \dot{F} = \int_V \dot{f}_s dV = \dot{f}_s V, \qquad G = \int_V g dV = gV.$$

Keeping this example in mind and now integrating the conservation equations obtained for n_h, n_e, $\rho\vec{v}$ $(\vec{v} \equiv \hat{r}v + \hat{z}w)$, p, and p_m over the volume of a Lagrangian cell, one obtains the following set of equations :

$$\frac{d}{dt}\int^V n_h dV = \frac{d}{dt}(n_h V) = \frac{d}{dt}(N_h)_{cell} = (\dot{N}_s)_{cell} \ , \tag{c.6}$$

$$\frac{d}{dt}\int^V n_e dV = \frac{d}{dt}(n_e V) = \frac{d}{dt}(N_e)_{cell} = (\dot{N}_e)_{cell} \ , \tag{c.7}$$

$$\begin{aligned} \frac{d}{dt}\int_V (\rho w) dV &= \frac{d}{dt}[M\langle w\rangle] \\ &= -\int_V (\frac{\partial p}{\partial z}) dV + m_s \int_V (w_s \dot{n}_s) dV \\ &= -(p - p^\infty) a_\perp + m_s \langle w_s\rangle \dot{N}_s \ , \end{aligned} \tag{c.8}$$

$$\begin{aligned} \frac{d}{dt}\int_V (\rho v) dV &= \frac{d}{dt}[M\langle v\rangle] \\ &= -\int_V \frac{\partial}{\partial r}(p + p_m) dV + m_s \int_V (v_s \dot{n}_s) dV \\ &= -2\pi Z \left[(p + p_m) r\right]_{r_{(k-1)}}^{r_{(k)}} + m_s \langle v_s\rangle \dot{N}_s \ , \end{aligned} \tag{c.9}$$

$$\begin{aligned} \frac{d}{dt}(\frac{pV}{\gamma - 1}) =& \dot{Q}_\parallel + \dot{Q}_\perp - \dot{Q}_{ioniz} \\ &- \int_V p(\nabla \cdot \vec{v}) dV + [\frac{kT_s}{\gamma - 1} + \frac{1}{2} m_s (\vec{v}_s - \vec{v})^2] \dot{N}_s \ , \end{aligned} \tag{c.10}$$

$$\frac{d}{dt}(p_m V) = \dot{Q}_{mgn} - \int_V p_m (\nabla \cdot \vec{v}) dV - \int_V \frac{\chi_m}{\mu_o} (\nabla B)^2 dV \ , \tag{c.11}$$

where $dV = 2\pi r dr dz$ is a volume differential, $V(k) = \pi(r_{(\ell)}^2 - r_{(\ell-1)}^2) z_{(k)}$ is the volume of a Lagrangian cell, $\langle v\rangle$ and $\langle w\rangle$ are the velocity components averaged over the volume of a Lagrangian cell, $a_{\perp(k)} = \pi(r_{(\ell)}^2 - r_{(\ell-1)}^2)$ is the lateral surface of cell "k", $\dot{Q}_\perp = \dot{Q}_{\perp(\ell)} - \dot{Q}_{\perp(\ell-1)}$, $\dot{Q}_{mgn} = \dot{Q}_{mgn(\ell)} - \dot{Q}_{mgn(\ell-1)}$, and, furthermore

$$\dot{Q}_{\parallel(k)} = q_e^\infty a_{\perp(k)} \ , \tag{c.12}$$

$$\dot{Q}_{\perp(\ell)} = 2\pi r_{(\ell)} z_{(k)} \chi_{e\perp} n_{(k)} k (\frac{\partial T}{\partial r})_k \ . \qquad (c.13)$$

The magnetic energy flux through the surface "ℓ" is given by

$$\dot{Q}_{mgn(\ell)} = 2\pi r_{(\ell)} z_{(k)} \chi_m (\frac{\partial p_m}{\partial r})_k \ . \qquad (c.14)$$

The flow work term appearing in the internal energy equation can be integrated over a cell volume:

$$\int_V p(\nabla \cdot \vec{v}) dV = p \int_V (\nabla \cdot \vec{v}) dV = p \int_S \vec{v} \cdot d\vec{\sigma} = p \frac{dV}{dt} \ . \qquad (c.15)$$

An analogous expression can be derived for the work spent on stretching the magnetic field lines in the direction normal to the magnetic field:

$$\int_V p_m (\nabla_\perp \cdot \vec{v}) dV = p_m (\frac{dV}{dt})_\perp = p_{m(k)} \frac{da_\perp}{dt} z_{(k)} \ . \qquad (c.16)$$

Since the magnetic field lines are assumed to remain straight and parallel all the time (infinitely long cylindrical plasmoid approximation with regard to the magnetic field topology), there is no work done by the magnetic field in the z direction. However, the volume integral of the magnetic field energy is continuously changing owing to the field volume swept by the plasmoid expanding along the field lines:

$$\dot{Q}_{swp(k)} = p_{m(k)} a_{\perp(k)} \frac{dZ_{(k)}}{dt} \ . \qquad (c.17)$$

This term must be taken into account in the equation written for the magnetic field energy.

(d) Working Equations

For a given set of initial values (initial mass, dimensions, density, and temperature given for each Lagrangian cell, the velocity components being assumed to be identical to zero at t = 0), the time evolution of the cloud state parameters are computed for the set of Lagragian cells on the basis of the following equations:

(a) Number of particles in the cells and cell masses:

$$N^{t+\Delta t}_{cell(k)} = n_{(k)} V_{(k)} = N^t_{cell(k)} + \dot{N}_{s(k)} \cdot \Delta t \quad , \qquad (d.1)$$

$$M_{cell(k)} = m_a n_{cell(k)} V_{(k)} = m_a N_{cell(k)} \quad . \qquad (d.2)$$

(b) Radial and axial velocity components of the respective cell boundaries:

$$\frac{d}{dt}(M_{(\ell)} v_{(\ell)}) = -2\pi Z_{(\ell)} \left[(p + p_m + q_v) r \right]_k^{k+1} + m_s v_s \dot{N}_s \ , \qquad (d.3)$$

$$\frac{d}{dt}(M_{(k)}w_{(k)}) = -a_{\perp(k)}\left[p + q_v\right]_k^{\infty} + m_s w_s \dot{N}_s \ , \qquad (d.4)$$

where k and ℓ are (radial) cell volume and cell boundary indices, respectively, and $M_{(\ell)}$ is the effective mass attached to the radial cell boundary considered (i.e. half of the total mass of the two cells separated by the boundary). Since the plasmoid expansion in the flux tubes along the magnetic field lines may be viewed as a constant-area channel flow with heat addition, the maxima of the respective parallel flow velocities are limited to the local sonic velocities.

The quantities q_v and q_w are the artificial viscosities defined in terms of the velocity gradients in such a manner as not to violate energy conservation principles [32]. The quantity $a_\perp$ represents the end-face area of a Lagrangian cell.

(c) Positions (coordinates) of the cell boundaries $R_{(\ell)}$, $Z_{(k)}$, cell volume $V_{(k)}$, and heavy-particle density $n_{h(k)}$:

$$R_{(\ell)}^{t+\Delta t} = R_{(\ell)}^{t} + \langle v \rangle \Delta t \ , \qquad (d.5)$$

$$Z_{(k)}^{t+\Delta t} = Z_{(k)}^{t} + \langle w \rangle \Delta t \ , \qquad (d.6)$$

where $\langle v \rangle$ and $\langle w \rangle$ denote time-centered values (the centered-time solution method is discused in the next section),

$$V_{(k)} = \pi\left(R_{(\ell)}^2 - R_{(\ell-1)}^2\right) Z_{(k)} \ , \qquad (d.7)$$

$$n_{(k)} = N_{cell(k)}/V_{(k)} \ . \qquad (d.8)$$

In the same computational sequence, the quantities

$$a_{\perp(k)} = \pi(R_{(\ell)}^2 - R_{(\ell-1)}^2) \ ,$$
$$a_{\parallel(k)} = 2\pi R_{(\ell)} Z_{(k)}$$

are updated.

(d) Artificial viscosity terms computed for the next time step (intrinsic cell properties):

$$q_{v(k)} = \begin{cases} c\rho(\Delta\ell)^2(\nabla_r \cdot \vec{v})^2, & \text{if } v_{(k+1/2)} \le v_{(k-1/2)} \\ 0, & \text{if } v_{(k+1/2)} > v_{(k-1/2)} \end{cases} \ , \qquad (d.9)$$

$$q_{w(k)} = \begin{cases} c\rho(\Delta\ell)^2(\nabla_z \cdot \vec{v})^2, & \text{if } w_{(k+1/2)} \le w_{(k-1/2)} \\ 0, & \text{if } w_{(k+1/2)} > w_{(k-1/2)} \end{cases} \ . \qquad (d.10)$$

Note that the indices $k + \frac{1}{2}$, $k - \frac{1}{2}$ denote cell boundaries (corresponding to the radial boundary indices ℓ, $\ell - 1$, respectively). Since the axial motion is

practically a vacuum expansion at all times, $q_{w(k)}$ remained zero in all practical scenario calculations. Furthermore, owing to the rapid pressure reduction in the peripheral plasmoid cells caused by axial expansion, the radial artificial viscosity altogether did not play any significant role either in the present calculations.

(e) Internal energy: cell pressure $p_{(k)}$ and/or temperature $T_{(k)}$:

The internal energy conservation equation can be reduced to the form

$$\frac{d}{dt}(p_{(k)}) + \gamma p_{(k)} \frac{1}{V_{(k)}} \frac{d}{dt}(V_{(k)}) = \frac{\gamma - 1}{V_{(k)}} [\dot{Q}_{\parallel} + \dot{Q}_{\perp} - \dot{Q}_{ioniz} - \dot{Q}_{src}] \ , \qquad (d.11)$$

where the terms appearing on the R.H.S. have been defined by eqs. (c.10), (c.12), and (c.13).

On the basis of this expression, an equation can be derived for the temperature distribution:

$$\frac{d}{dt}(T_{(k)}) = A \frac{\partial}{\partial r}(r n_h k \chi_{\perp} \frac{\partial T_{(k)}}{\partial r}) + B T_{(k)} + C \ , \qquad (d.12)$$

where

$$A = 2\pi Z (\frac{\gamma - 1}{1 + \alpha})(\frac{1}{n_h k})(\frac{1}{V}) \ ,$$

$$B = -(\gamma - 1)\frac{1}{V}\frac{dV}{dt} - \frac{1}{N_{cell}}\frac{dN_{cll}}{dt} \ ,$$

$$C = (\frac{\gamma - 1}{1 + \alpha})(\frac{1}{n_h k})(\frac{1}{V})[\dot{Q}_{\parallel} + \dot{Q}_{ionz} + \dot{Q}_{src}] \ .$$

Equation (d.12) can readily be solved for $T_{(k)}$ by means of an implicit algorithm.

Note that, because of the centered-time discretization scheme used, the volumetric dilution term $\frac{1}{V}\frac{dV}{dt}$ appearing in the above expression is a known quantity here.

(f) Electron density and ionization degree:

The rate equation

$$\frac{dn_e}{dt} = \dot{n}_e - n_e \frac{1}{V}\frac{dV}{dt} = (\beta_{3b} n_e + \beta_{\nu})(n_{es}^2 - n_e^2) - n_e \frac{1}{V}\frac{dV}{dt} \qquad (d.13)$$

that can be obtained from eqs. (b.2) and (b.17) is solved in two steps: first the electron density change due to ionization and recombination is calculated and the result thus obtained is corrected for volumetric dilution.

Indeed, if collisional processes dominate over radiative ones, an integral of the above equation yields (the volumetric dilution term is neglected for the time being, $n_{e_S} \equiv n_{e_S}(t + \Delta t)$)

$$\left.\frac{n_{e_1}}{n_{e_S}}\right)_{coll} = \left[\frac{exp(\Delta t/\tau_{inz})}{exp(\Delta t/\tau_{inz}) + (n_{e_S}/n_{e_o})^2 - 1}\right]^{1/2} , \qquad (d.14)$$

where $\tau_{inz} \equiv (2\beta_{3b} n_{e_S}^2)^{-1}$ is the effective ionization/recombination time associated with collisional processes and n_{e_o} is the initial electron density. An effective (constant) value is used here for the rate coefficient β_{3b}: $\beta_{3b} = \beta_{3b(\langle T \rangle)}$, where $\langle T \rangle$ is the effective temperature for the time interval t, $t + \Delta t$. As can be seen,

$$\text{if} \quad \frac{\Delta t}{\tau_{inz}} \ll 1, \quad \text{then} \quad n_{e(t+\Delta t)} \rightarrow n_{e(t)} \; ;$$

$$\text{if} \quad \frac{\Delta t}{\tau_{inz}} \gg 1, \quad \text{then} \quad n_{e(t+\Delta t)} \rightarrow n_{e_S(t+\Delta t)} \; .$$

A similar expression can be obtained if radiative processes dominate:

$$\left.\frac{n_{e_1}}{n_{e_S}}\right)_{rad} = \frac{exp(\Delta t/\tau_{inz}) - (n_{e_S} - n_{e_o})/(n_{e_S} + n_{e_o})}{exp(\Delta t/\tau_{inz}) + (n_{e_S} - n_{e_o})/(n_{e_S} + n_{e_o})} , \qquad (d.15)$$

with $\tau_{inz} \equiv (2\beta_\nu n_{e_S})^{-1}$ in this case. If both collisional and radiative processes are relevant, the ionization rate equation must be integrated numerically.

In a second step, the volumetric dilution is taken into account by correcting n_{e_1} for the same time increment Δt (see section **Numerical Scheme**):

$$n_e = n_e(n_{e_1}, \frac{1}{V}\frac{dV}{dt}) \; . \qquad (d.16)$$

The neutral particle density and the ionization degree are given by

$$\begin{aligned} n_a &= n_h - n_e \; , \\ \alpha &= n_e/n_h \; . \end{aligned} \qquad (d.17)$$

Once the particle densities are known, the collision frequencies ν_{ea} and ν_{ei} can be calculated, and, finally, the electrical conductivity σ and the resistive diffusion coefficient χ_m are determined:

$$\sigma_{(k)} = \frac{n_{e(k)} e^2}{m_e(\nu_{ea} + \nu_{ei})_\ell} , \qquad (d.18)$$

$$\chi_{m(k)} = (\mu_o \sigma_{(k)})^{-1} \; . \qquad (d.19)$$

(g) Magnetic pressure p_m and magnetic field strength B.

The equations obtained for the specific magnetic field energy p_m and the magnetic field strength B can be rewritten as

$$\frac{d}{dt}(p_m V) = \dot{Q}_{mgn} - p_m Z \frac{da_\perp}{dt} + p_m a_\perp \frac{dZ}{dt} , \qquad (d.20)$$

$$\frac{d}{dt}(BV) = \dot{Q}_B + B a_\perp \frac{dZ}{dt} . \qquad (d.21)$$

The expression for $\dot{Q}_B$ is analogous to eq. (c.14), except that p_m is expressed in terms of B.

The last term of the R.H.S. of these equations correspond to "volume sweeping" along the magnetic field lines.

Equation (d.20) can be reduced to the following expression ($V = a_\perp Z$):

$$a_\perp Z \frac{dp_m}{dt} + 2 p_m Z \frac{da_\perp}{dt} = \dot{Q}_{mgn},$$

i.e.

$$\frac{d}{dt}(p_m a_\perp^2) = \frac{a_\perp}{Z} \dot{Q}_{mgn} , \qquad (d.22)$$

which can be integrated for the $\frac{dZ}{dt} = 0$, $\sigma \to \infty$, $\left(\dot{Q}_{mgn} \to 0\right)$ case: $a_\perp^2 p_m =$ const; which means in a single-cell aproximation $R^4 B^2 =$ const or, as well, $R^2 B =$ const, where R represents the cell (plasmoid) radius. This is the condition of flux conservation in a fully ionized , infinitely conducting plasma (frozen-in field). The same information can be obtained from the equation for the volume integral of the magnetic field $(B * V)$.

On the other hand, in a cold neutral cloud one has $\sigma \to 0$, and the magnetic field instantaneously penetrates the gas (i.e. the gas sweeps the volume, in both the axial and radial directions, without "noticing" the presence of a magnetic field) and thus p_m and B remain unchanged there. Hence, the magnetic energy flux that assures the persistence of the $dp_m/dt = 0$ condition within the cloud (see eq. (d.20)) is given by

$$\dot{Q}_{mgn} = 2 p_m Z \frac{da_\perp}{dt} . \qquad (d.23)$$

In a general case, the resistive diffusion equations represented by eq. (d.20) or (d.21) are second-order differential equations. Owing to the integrals taken over the volumes of the Lagrangian cells (divergence theorem), these equations appear here as first-order equations. Their solution is be described in the next section.

Note that condition (d.23) applies during the initial phase of the cloud expansion. As soon as the outer cloud layers become conductive, two domains can be distinguished in the cloud. The interface or boundary separating these two domains propagates inward with the ionization front. The two domains are as follows:

a) the outer resistive conduction domain in, which the magnetic field (or magnetic pressure) distribution is calculated by solving the respective diffusion equation;

b) the inner cold core with $\sigma \rightarrow 0$, $\chi_m \rightarrow \infty$ with instantaneous field redistribution. In this region, the magnetic energy increment defined as $(\dot{Q}_{mgn} \cdot \Delta t)_{boundary}$ is instantaneously redistributed over the entire cold core without solving the diffusion equation. Practically, this means that eq. (d.22) is solved for the given source term represented by its R.H.S.. In this procedure, the entire cold core is considered to be a single (Lagrangian) cell.

(e) Numerical Scheme

(e1) Time centering and advancement of the velocities and coordinates

The working equations in their Lagrangian representation, as given above, represent a set of simultaneous equations which are to be solved in space and time. The numerical scheme used for solving these equations is based on splitting these equations into two groups and advancing them sequentially in time.

The first group consists of the momentum equations, which are the first to be solved, thus advancing the velocity values from the time level $n - 1/2$ to $n + 1/2$: $v^{n-1/2} \rightarrow v^{n+1/2}$, $w^{n-1/2} \rightarrow w^{n+1/2}$. The second group consists of the coordinates of the cell boundaries r, z, and of all intrinsic cell properties calculated (n_h, n_e, T, B, p, p_m, etc.).

Owing to the fact that the time increment $\Delta t = t_{n+1} - t_n$ may vary from time step to time step (the time step control will be discussed later), it is necessary to define the value of the quantities entering the R.H.S. of the momentum equations (d.3) and (d.4) at a "centered time" t_c. Note that (see Fig. 1b)

$$t_{n+1/2} - t_c = t_c - t_{n-1/2} \ ,$$

$$\text{whereas} t_{n+1} - t_{n+1/2} \neq t_n - t_{n-1/2} \ .$$

Hence, noting that

$$\Delta t_c = 1/2\Delta t_o + 1/2\Delta t \qquad (e.1)$$

and

$$t_c - t_{n-1/2} = \frac{1}{2}\Delta t_c = \frac{1}{4}(\Delta t_o + \Delta t) ,$$

$$t_c - t_{n-1} = \frac{1}{2}(\Delta t_o + \Delta t_c) = \frac{3}{4}\Delta t + \frac{1}{4}\Delta t ,$$

we obtain in linear approximation for the time variation of the function f the following expression:

$$\frac{f^{nc} - f^{n-1}}{f^n - f^{n-1}} = \frac{t_{nc} - t_{n-1}}{t_n - t_{n-1}} = \frac{3}{4} + \frac{1}{4}(\frac{\Delta t}{\Delta t_o}) , \qquad (e.2)$$

i.e. the value of the function f^{nc} at the centered time t_c is given by

$$f^{nc} = c_f^{(-)} f^{n-1} + c_f^{(o)} f^n , \qquad (e.3)$$

where the factors $c_f^{(-)} = \frac{1}{4}(1 - \frac{\Delta t}{\Delta t_o})$ and $c_f^{(o)} = \frac{1}{4}(3 + \frac{\Delta t}{\Delta t_o})$ are the weighting factors of the function values at time levels $n-1$ and n, respectively.

Once the velocity values at the time level $n+1/2$ are known (centered time between the levels n and $n+1$), the cell boundary coordinates r and z and all geometric functions ($a_\parallel$, $a_\perp$, V, etc) can be advanced from t^n to t^{n+1}.

The artificial viscosities $q_{v(k)}$ and $q_{w(k)}$ as given by eqs. (d.9) and (d.10) are also calculated here. The constant c appearing in these equations is of the order of unity. In our calculations $c = 4$ is used.

Hence, the solution of the momentum equations is based on an explicit scheme that involves the time-centered values of the respective derivatives.

(e2) Intrinsic cell properties

Next, the heavy-particle density is calculated by dividing the total number of particles in the cell, according to eq. (d.1), by the updated volume.

The advancement in time of some of the intrinsic cell properties from the time level t^n to t^{n+1} involves implementation of an implicit numerical scheme. Here, we describe in detail the algorithm used in advancing the temperature and the magnetic field diffusion equations.

Expanding the temperature equation (d.12) and collecting terms, we obtain an expression of the form

$$a_k \hat{T}_{k-1} + b_k \hat{T}_k + c_k \hat{T}_{k+1} = d_k , \qquad (e.4)$$

where the "hats" denote the values advanced to the time level $n+1$ and

$$a_k = -\frac{A\Delta t f}{r_{k+1} - r_{k-1}} \left(\frac{rnk\chi^\perp}{r_k - r_{k-1}} \right)_{\ell-1} ,$$

$$b_k = 1 + \frac{A\Delta t f}{r_{k+1} - r_{k-1}} \left[\left(\frac{rnk\chi^{\perp}}{r_{k+1} - r_k} \right)_{\ell} + \left(\frac{rnk\chi^{\perp}}{r_k - r_{k-1}} \right)_{\ell-1} \right] + B\Delta t f \ ,$$

$$c_k = + \frac{A\Delta t f}{r_{k+1} - r_{k-1}} \left(\frac{rnk\chi^{\perp}}{r_{k+1} - r_k} \right)_{\ell} \ ,$$

$$d_k = T_k + \frac{A\Delta t(1-f)}{r_{k+1} - r_{k-1}} \left[(rnk\chi^{\perp})_{\ell} \left(\frac{T_{k+1} - T_k}{r_{k+1} - r_k} \right) - (rnk\chi^{\perp})_{\ell-1} \left(\frac{T_k - T_{k-1}}{r_k - r_{k-1}} \right) \right] + (1-f)B\Delta t T_k + C\Delta t \ .$$

In eq. (e.4) f is an implicity factor defined by the equation

$$\tilde{T}^{\alpha} = \alpha f \hat{T} T^{\alpha - 1} + (1 - \alpha f) T^{\alpha} \ , \qquad (e.5)$$

where $\tilde{T}$ is the variable linearized in time, whereas T and $\hat{T}$ are the variables at the old and new times, respectively. The quantity α represents an arbitrary (given) exponent (in the case of eq. (e.4) α is unity). In our calculations, an implicity factor of $f = 0.5$ (combined with the centered time scheme) was used, which is equivalent to the Crank-Nicolson scheme. For the value of f employed in our calculations, this scheme is unconditionally stable.

Note that eq. (e.4) is valid for $3 \leq k \leq LE1$. At the cloud boundaries (inner boundary: $r_{(2)} = 0$; outer boundary: $r_{(LE1)} = R_{cld}$) we require the following boundary conditions to be satisfied: at the axis ($r = 0$, $\ell = 2$), the Neumann condition $\partial T / \partial r = 0$ is to be satisfied, which, in view of eq. (e.4), yields

$$b_2 \hat{T}_2 + c_2 \hat{T}_3 = d_2 \ , \qquad (e.6)$$

where $b_2 = (a_2 + b_2)$.

At the outer boundary ($r > R_{(\ell = LE1)}$), we apply the Dirichlet condition $T = \text{const} = T^{\infty}$, which, when substituted in eq. (e.4), yields

$$a_{LE1} \hat{T}_{LE2} + b_{LE1} \hat{T}_{LE1} = d_{LE1} - c_{LE1} T^{\infty}_{LE} \ . \qquad (e.7)$$

Equations (e.4), (e.5) and (e.6) form a closed, tridiagonal set of simultaneous equations. In matrix form , this set can be written as

$$\begin{pmatrix} b_2 & c_2 & 0 & 0 & 0 & 0 & 0 \\ a_3 & b_3 & c_3 & 0 & 0 & 0 & 0 \\ 0 & \dots & \dots & \dots & 0 & 0 & 0 \\ 0 & 0 & a_k & b_k & c_k & 0 & 0 \\ 0 & 0 & 0 & \dots & \dots & \dots & 0 \\ 0 & 0 & 0 & 0 & a_{LE2} & b_{LE2} & c_{LE2} \\ 0 & 0 & 0 & 0 & 0 & a_{LE1} & b_{LE1} \end{pmatrix} \begin{pmatrix} T_2 \\ T_3 \\ \dots \\ T_k \\ \dots \\ T_{LE2} \\ T_{LE1} \end{pmatrix} = \begin{pmatrix} d_2 \\ d_3 \\ \dots \\ d_k \\ \dots \\ d_{LE2} \\ d_{LE1} \end{pmatrix} \ , \qquad (e.8)$$

whose inversion yields the solution set for T_k, $2 \leq k \leq LE1$.

Next, the magnetic field diffusion equation is solved and B is advanced: $B^n \rightarrow B^{n+1}$. Here, we have the option to solve the conservation equation given for the magnetic pressure p_m, eq. (d.20), or to solve the equivalent equation given for B (d.21):

$$\frac{d}{dt}(Ba_\perp) = \frac{2\pi}{r_k - r_{k-1}}\left[r_\ell \chi^m_\ell (B_{k+1} - B_k) - r_{\ell-1}\chi^m_{\ell-1}(B_k - B_{k-1})\right] , \quad (e.9)$$

where the magnetic diffusivity values χ^m, which are intrinsic (volume-bound) properties are evaluated at the cell surfaces (an exception: the plasma boundaries where the last cell properties are used).

It was pointed out above (see **Working Equations**) that the resistive diffusion equation for B is solved in two domains: (i) an outer resistive conductive domain for which eq. (e.9) is valid, and (ii) a transient unionized, nonconductive core region for which instantaneous field redistribution is assumed for the given source term appearing on the R.H.S. of eq. (d.21).

In the ionized region, eq. (e.9) is recast in the form of eq. (e.4):

$$a_k \hat{B}_{k-1} + b_k \hat{B}_k + c_k \hat{B}_{k+1} = d_k , \quad (e.10)$$

where

$$a_k = -\frac{f}{a_\perp}\frac{2\pi\Delta t}{r_k - r_{k-1}}(r\chi^m)_{\ell-1} ,$$

$$b_k = 1 + f\Delta a_\perp + \frac{f}{a_\perp}\frac{2\pi\Delta t}{r_k - r_{k-1}}\left[(r\chi^m)_\ell + (r\chi^m)_{\ell-1}\right] ,$$

$$c_k = -\frac{f}{a_\perp}\frac{2\pi\Delta t}{r_k - r_{k-1}}(r\chi^m)_\ell ,$$

$$d_k = B_k - (1-f)B_k\Delta a_\perp + \frac{(1-f)}{a_\perp}\frac{2\pi\Delta t}{r_k - r_{k-1}}\left[(r\chi^m)_\ell (B_{k+1} - B_k) - (r\chi^m)_{\ell-1}(B_k - B_{k-1})\right] .$$

Equation (e.10) is valid for the domain $LMC \leq k \leq LE1$. Here, the lower index LMC refers to the "last magnetized cell" of the plasmoid. Physically, this is the last ionized cell in contact with the cold unionized core region. This equation is supplemented by Dirichlet-type boundary conditions at both boundaries (inner boundary: $B_{LMC-1} = \text{const} = B_{core}$, outer boundary: $B_{LE} = \text{const} = B_o$). These two boundary conditions close the system of equations for the ionized region.

The solution of eq. (e.10) again involves the inversion of a three-diagonal matrix of the form (e.8) as done in the solution of the temperature equation (e.4).

The unionized region defined by $2 \leq k \leq LMC - 1$ is treated as a single cell for which the magnetic flux is calculated by explicitly solving the magnetic pressure equation (d.22) with the given source term represented by the R.H.S. of this equation.

The time advancement of the electron density is done in two steps. First the source term $\dot{n}_e$ is computed on the basis of the known values of the new equilibrium (Saha) electron density $n_{es}^{n+1} = n_{es}(T^{n+1}, n_h^{n+1})$ and then the rate coefficients β_{3b}, β_ν, are evaluated at the intermediate temperature value $(T^{n+1/2})$. The electron density increment associated with the finite-rate ionization and recombination processes $\Delta n_{e_1} = n_{e_1} - n_{e_o} = \dot{n}_e \Delta t$ is computed (see eqs. (b.15), or (d.14) to (d.16)) without considering volumetric dilution. This value Δn_{e_1} is checked against some physical constraints (for example, $n_{e_o} \leq n_{e_1} \leq n_{es}^{n+1}$ if ionization dominates, $n_{es}^{n+1} \leq n_{e_1} \leq n_{e_o}$ if recombination dominates; the ionization energy associated with the production of Δn_{e_1} electrons may not be larger than the energy input to the cloud during the time increment Δt, etc.). If necessary, the calculated Δn_{e_1} is corrected in accordance with the physical constraints imposed. The actual source strength is then defined as $\dot{n}_e = (\Delta n_{e_1}/\Delta t)_{corr}$ and inserted back into eq. (d.13). In a second step, this equation is now solved for the updated value of the electron density $\hat{n}_e$ in accordance with the scheme

$$\hat{n}_e - n_e = \left[f_e \hat{n}_e + (1 - f_e) n_e\right] \left(\frac{\Delta V}{\langle V \rangle}\right)_n^{n+1} (\Delta n_{e_1})_{corr} \, . \qquad (e.11)$$

The factor f_e appearing in this equation is an implicity factor ($f_e = 0.5$ is used throughout the calculations).

(e3) Time step control

In solving the kinematic equations (momentum equations, coordinates, and all geometrical functions depending on these quantities) it was made certain that the time step used satisfies the standard Courant-Fridrichs-Lewy condition

$$\left[\frac{c\Delta t}{|r^{n+1} - r^n|}\right]_{max} \leq 1 \, ,$$

$$\left[\frac{c\Delta t}{z_{n+1} - z_n}\right]_{max} \leq 1 \, ,$$

where c denotes the local sonic velocity.

The whole computational domain (i.e. all Lagrangian cells) was scanned after each time step to locate the respective maxima of the above quantities. A more stringent condition imposed empirically on the percentage change of

the individual variables during a time step, $|\Delta f/\langle f\rangle| \leq y_{max}$, usually replaced the C.F.L. condition. As a matter of fact, in the neighborhood of the radial velocity reversal point with $v \rightarrow 0$, the C.F.L. condition had to be switched off altogether. A value of $y_{max} = 10^{-3}$ is used throughout the calculations.

Excmpt from this condition were the variables which, owing to their smooth variation in time (the axial expansion velocity, etc.), did not affect either the stability of the numerical system or the accuracy of the calculations. The variables that played a significant role in determining (reducing) the applicable time step were the radial velocity (owing to the $\vec{j} \times \vec{B}$ deceleration and the subsequent Alfvén oscillations) and the temperature (because of the sensitivity of the ionization rate to the temperature changes).

As a result of these conditions, the average time step applicable to modeling the cloud evolution scenarios presented was $\approx 10^{-11}$ s. The typical CPU time required for a run on a CRAY-XMP2 computer (with 22 Lagrangian cells applied) was of the order of 1 min to 2 min.

(e4) Integral checks

To check the effect of round-off errors on the accuracy of calculations, the conservation equations considered - including the total energy equation - were integrated in time and space independently of the sequence of time advancements applied to the individual variables. At the end of the computer run, the results thus obtained were compared with values obtained with the help of the numerical scheme applied. The total error accumulated in 2 to 5 times 10^5 cycles was typically under 5 % for the calculated variable values.

IV. RESULTS OF CALCULATIONS

(a) Plasmoid Evolution: Analysis of a Representative Scenario

As a representative or reference case we shall consider a scenario with the following set of initial parameter values:

Background plasma temperature	:	T_e^{∞}	$= 5\ keV$
Background plasma density (D^+)	:	n_e^{∞}	$= 10^{19}\ m^{-3}$
Magnetic field strength	:	B_o	$= 2.5$ tesla
Total number of D^o particles deposited in the half-cloud (corresponds to half of a spherical pellet of $r_p = 0.5$ mm)	:	N_{htotl}	$= 1.6 \times 10^{19}$
Duration of particle deposition	:	τ_{src}	$= 20\ \mu s$

Temperature of particles deposited : $T_s = 15\ ^oK$
Density of particles deposited : $n_s = 6 \times 10^{28}\ m^{-3}$
Velocity of the source particles : $v_s = 0\ m/s.$

To assure well-defined initial cloud dimensions and parameter values, it is assumed that 5 % of the total number of particles given above are instantaneously deposited. The deposition radius (= initial cloud radius) is equal to the radius of the equivalent spherical pellet specified. It was found in numerous check runs that the exact value of this initial and instantaneously deposited mass has no significant effect on the final results as long as it is kept small in relation to the total mass. Following the instantaneous deposition of 5 % of the particles, the residual mass is deposited within the time τ_{src} at a constant rate: $\dot{N} = N_{rest}/\tau_{src}$.

The variation of some representative quantities, such as the total number of heavy particles ($D^o + D^+$) present in the half-cloud, the cloud radius, the average cloud temperature and cloud density, the average ionization degree, and the total magnetic flux enclosed by the cloud, are shown in Fig. 2 for the first 25 μs of the cloud evolution. Note that all average or bulk cloud/plasmoid characteristics referred to hereafter are defined as mass-averaged quantities:

$$\langle f \rangle = f_{avr} = \sum_{k=1}^{cell} N_{cell}(k) \cdot f_{cell}(k) \ / \ \sum_{k=1}^{cell} N_{cell}(k) \ ,$$

where $N_{cell}(k) = N_{cell}(k,t)$ represents the number of particles in a Lagrangian cell k at any given time instant, and the summation is taken over all cells representing the cloud (or plasmoid).

As can be seen, the mass of the cloud continuously increases until $\tau = 20\ \mu s$, and the bulk ionization degree reaches ~ 1.0 at $\tau \approx 16\ \mu s$, remaining at this value for the rest of the mass addition phase. The radius of the cloud reaches a "quasi-steady" value of ~ 5 mm in about 1 μs (the ionization time of the outer plasmoid layer).

The bulk plasmoid density decreases exponentially during the first expansion phase but changes relatively slowly for times $\tau \gtrsim 5\ \mu s$. The bulk plasmoid temperature sharply increases during the first expansion phase (the kinetic energy only slowly increases because of inertia effects) and, owing to gasdynamic expansion and ionization processes, changes relatively slowly during the subsequent mass addition phase. The enclosed magnetic flux rapidly increases as long as the outer cloud layers remain unionized (volume sweeping), and remains practically constant (frozen-in) afterwards. A slow increase of the enclosed magnetic flux can be observed at later times, which is due to magnetic field rediffusion. Figure 3 shows the time development of the radial temperature and

density distributions for the first 25 μs. The temperature profile remains hollow during the entire time period considered (note the logarithmic time scale), while the particle density distribution has its maximum at the axis of the flux tube. The density profile gets filled up in the course of time. (Note that the plasma temperature is not displayed in either this or any of the following plots.) Since all major changes that determine the "quasi-steady" characteristics of the plasmoid are completed during the initial expansion phase associated with the ionization of the outer cloud layers, some Alfvén oscillations, and the full stop of the radial expansion, we shall consider this initial phase in somewhat greater detail. Figures 4, 5, and 6 show the radial distributions of the major plasmoid characteristics at three times: $\tau \approx 1\ \mu s$, $\tau \approx 2\ \mu s$, and $\tau \approx 3\ \mu s$, respectively. One may observe the velocity reversal at the plasmoid periphery in Fig. 5 and the practically full stop of the radial expansion in Fig. 6 (the oscillatory motion of the outermost plasmoid layer still continues). The heavy-particle density decreases rather rapidly at the plasmoid axis. The temporal variation of the electron density distribution is defined by respective heavy-particle density and temperature distribution curves. The longitudinal extent (half-length) of the Lagrangian cells along the magnetic field lines is shown in Fig. 7, where the temperature and heavy particle distributions are plotted for the time t = 5 μs (the $z = 0$ plane is a symmetry plane). As can be seen, the peripheral plasmoid layers are heated faster and thus expand at a rate considerably higher than do the interior ones.

The length-to-diameter ratios of cloud regions with ionization degrees of less than 0.99 are tabulated in Table 1 for the time at which the maximum radius is reached for a variety of experimental conditions. The cloud region in which the particles are not yet fully ionized is the source region of H_α radiation emission. Hence the length-to-diameter ratios shown here can be compared with experimentally observed values. As can be seen, under very different scenario conditions (the number of particles deposited changes by two orders of magnitude, the applied magnetic field strength by a factor of 4) the length-to-diameter ratio of the not fully ionized fraction of the cloud varies between 2 and 5. These values are in good agreement with the cloud geometries observed in pellet experiments (see, for example, the CCD and framing camera pictures of Durst [25], or the striations presented by Wurden et al. [34]).

Table 1. Length-to-diameter ratio of the not fully ionized region ($\alpha \leq 0.99$, region of possible H_α radiation emission) at the moment when the maximum cloud radius is reached for different ablation scenarios.

a) The total number of particles N deposited within $\tau_{src} = 20\ \mu s$ is varied*.

* All other conditions are identical to those specified for the "representative

N	L/D (5 keV)
2.0×10^{18}	2.3
5.5×10^{18}	3.7
1.6×10^{18}	4.4
4.4×10^{19}	4.9
1.3×10^{20}	4.9

b) The applied magnetic field strength B_o and plasma temperature are varied*.

B(tesla)	L/D (5 keV)	L/D (7 keV)
1.0	2.3	2.1
2.0	3.7	3.4
3.0	4.4	4.2
4.0	4.9	4.9

(b) Radial Structures

Owing to the fact that in the multi-cell Lagrangian approximation used only the outermost plasmoid layer (the outer Lagrangian cell) is in direct contact with the plasma in the radial direction, a conductive heat wave followed by an ionization wave is expected to propagate from the plasmoid periphery toward the symmetry axis. At the same time, since the peripheral cells are being heated at a higher rate than the central ones, they expand in the axial direction, thus causing a rapid density reduction at the plasmoid periphery. There are thus two counteracting physical processes acting at the plasma periphery: the stopping and the pile-up of the outward-streaming high-density cloud layers at the ionization radius; the high axial expansion and density reduction rates produced there by the enhanced heat input and the resulting higher temperatures and the associated higher pressure gradients along the magnetic field lines. As has been mentioned in the model description, the axial flow velocity is limited to the local sonic velocity a: $w_z = \min(w_z, a)$. Without this limitation, the density reduction due to axial expansion in the peripheral plasmoid layers could be still faster. A time sequence of distributions of the radial heavy-particle density, and temperature, ionization degree, and electron density is shown in Figs. 8 to 11 for the representative case discussed in the previous section. As can be seen, the heavy particle density distribution remains qualitatively "self-similar"

---

case".

during the entire expansion phase: it peaks all the time at the center and monotonically decreases toward the periphery. Hence density reduction due to axial expansion not only balances but also overrides the pile-up of the mass at the ionization radius. This distribution is contrasted by the inverted (hollow) temperature profile (see Fig. 9), the temperature remaining all the time highest at the plasmoid boundary and lowest at the axis of symmetry. Obviously, the ionization degree distribution that corresponds to these density and temperature profiles will be similar to the temperature curve with maximum at the plasmoid boundary and minimum at its centerline (Fig. 10). The time sequence of the ionization degree distribution curves clearly reproduces the inward motion of a cylindrical ionization front. It is of interest to see what the structure of the electron density distribution corresponding to the given spatial plasmoid characteristics looks like: is it identical with the ionization degree profile?

As can be seen from Fig. 11, the peak of the electron density maximum remains all the time shifted to the left of the locus of the ionization degree maximum, i.e. to the side with lower temperature and higher heavy-particle density. In this example, the peak value of the electron density remains approximately constant ($\sim 10^{24}\ m^{-3}$), while its position is being continuously shifted toward the center of the plasmoid. In the wake of the electron density curve, i.e. on the high-temperature side of the electron density peak, the electron density decreases, both in time and space, because of the axial expansion effects. At the locus of the electron density maximum, the plasmoid is not yet fully ionized. Hence the expanding cloud displays a rather characteristic structure during the first phase of its expansion: hollow temperature profile associated with an inward-bound thermal wave (temperature, ionization degree), and an electron density peak that precedes the ionization wave. As time goes on, the temperature distribution becomes more and more filled up at the plasmoid axis and the electron density distribution, once its peak (or the ionization front) reaches the plasmoid axis, becomes identical to the heavy-particle distribution. The time evolutions of the radial temperature, heavy-particle density, electron density, and m.f. strength are reproduced in Figs. 12 and 13 in a continuous manner for the first 5 μs of the cloud expansion time. Here one can follow the temporal variation of the plasmoid radius up to its maximum value (ionization radius) and the inward propagation of the ionization wave as well. One can clearly see the growth of the cloud radius up to a time $\simeq 1\ \mu s$, the hollow temperature profile and the transition to a quasi-steady heavy-particle density profile. The electron density distribution initially displays a deep hole at the plasmoid axis (for technical reasons, a lower limit was imposed on the electron densities plotted ($10^{16}\ m^{-3}$); the actual electron density approaches zero in this region). This "hole" first expands together with the cold gas volume and

then, after the heat flux also penetrates the central plasmoid region, it is filled up. After full ionization is reached, the electron density profile becomes identical to the heavy-particle density profile. The enclosed magnetic field remains spatially uniform and constant in time as long as the cloud remains unionized and expands unaffected by the presence of the magnetic field. Once the outer layer becomes ionized, the enclosed magnetic field is practically frozen in, and the variation of the interior magnetic field strength is now governed by the motion (volumetric change) of the plasma boundary. As can be seen from Fig. 13, the magnetic field strength rapidly decreases in time as the plasmoid radius approaches its maximum value, and the follows the overdamped compressive oscillations of the plasmoid boundary as the transition to the quasi-steady state takes place. At the same time, rediffusion of the magnetic field sets in at the plasmoid boundary. Since the initial plasmoid temperature (electrical conductivity) is rather low, the rediffusion is rather rapid at the begining and becomes rather slow (measured on the resistive diffusion time scale) at later times.

(c) Effect of the Number of Particles Deposited
(Ablation Rate Effects)

In a series of runs, the number of particles deposited was varied within the interval $2 \times 10^{18} < N_{half} < 2 \times 10^{20}$ at a fixed particle deposition (source duration) time: $\tau_{src} = 20\ \mu s$. All other plasma and pellet conditions corresponded to the reference case discussed above. Owing to the fixed source duration, the results may be viewed as those reflecting pellet ablation rate effects.

Figure 14 shows the variations of the maximum plasmoid radii attained, as well as the radii after evolution times of 10 μs and 20 μs as functions of the number of particles deposited. The times at which the maximum radii were reached are also displayed on the respective curves. Owing to inertia effects, the maximum radius is usually larger than its equilibrium value. This quasi-steady equilibrium value is then reached during the subsequent longitudinal expansion phase. The curves displayed clearly show the effect of the deposited mass (or ablation rate) on the cloud size in the transverse direction: the cloud radius increases with increasing number of particles deposited . This is so because it takes longer to ionize a larger number of neutral particles and thus the cloud has a longer time to expand before interaction with the magnetic field begins. Note that in all these cases the mass source is active for 20 μs. Nevertheless, the growth of the cloud radius stops as soon as the outer cloud layers start to become ionized. As of this time, the particles fed to the cloud expand in the axial direction. Figure 15 shows the bulk (mass-averaged) temperature of the plasmoid for two time instants: at the time when the transverse expansion

is stopped ($R = R_{max}$) and after 10 μs of the cloud evolution. As could be expected, the bulk temperature notably decreases with increasing cloud mass (or ablation rate). The corresponding density variation with cloud mass and expansion time is shown in Fig. 16. Here, too, the mass dependence is clearly visible. The variation of the bulk ionization degree at the moment of radial confinement ($v_\perp = 0$, $R = R_{max}$) with the cloud mass is shown in Fig. 17. It is noteworthy that the radial expansion of the plasmoid comes to a full stop at relatively low average ionization degree values. Of course, the outer Lagrangian cell(s) is(are) already ionized at this time.

The effect of the cloud mass on its diamagnetic characteristic is shown in Fig. 18. Here the enclosed magnetic field is shown as a function of the total number of particles deposited. As can be seen, at the moment of radial confinement ($\tau = \tau_{(R=R_{max})}$) the trapped magnetic field decreases with increasing cloud mass. This is a consequence of the larger initial radial momentum gained at lower initial temperatures (the ionization takes longer): after a frozen-in state is reached at the plasma periphery, the expanding neutral core is still pushing this ionized layer outward, thus further reducing the average magnetic field inside the cloud. The curves corresponding to $\tau = 10$ μs and $\tau = 20$ μs show the effects of rediffusion of the magnetic field and of the gradual reduction of the plasmoid radius (caused by axial expansion).

The effect of the mass source strength (or ablation rate) on the plasmoid characteristics may also be checked by fixing the total number of particles to be deposited and by varying the duration of the deposition. In a series of calculations τ_{src} was varied from 0 μs to 30 μs, while $N_{half} = 1.6 \times 10^{19}$ ($T_e^\infty = 5$ keV) was kept constant. In another series of runs, $N_{half} = 1.3 \times 10^{20}$ with $T_e^\infty = 4.3$ keV was assumed. The corresponding variation of the maximum plasmoid radii obtained is displayed for the first case in Fig. 19 ($N = 1.6 \times 10^{19}$), while the plasmoid radii at $\tau(R = R_{max})$, $\tau = 10$ μs, and $\tau = 20$ μs obtained for the second case ($N = 1.3 \times 10^{20}$, $T_e^\infty = 4.3$ keV) are given in Fig. 20. The rest of the pellet and plasma parameters used as input in these computer runs are identical to those of the reference case. The behavior is as expected on the basis of Figs. 14 to 17. Note that $\tau_{rsc} = 0$ corresponds to instantaneous particle deposition. As can be seen, instantaneous particle deposition results in the largest cloud radius that can be obtained with the given number of particles deposited (under identical plasma conditions). At moderate source strengths, the cloud radius produced varies only weakly with the source duration.

(d) Heat Flux (*Background Plasma Temperature*) and Magnetic Field Effects

The heat flux affecting the cloud determines the initial rate of increase of

the pressure in the absorbing cloud layers and thus the force driving the cloud expansion. Also the rate of ionization of the neutral particles is a function of the incident heat flux. On the other hand, the magnetic field strength in combination with the cloud expansion velocity determines the force that counteracts the expansion of the ionized layers and brings the transverse expansion of the plasmoid to a full stop. A balance between these two effects determines the stopping radius as well as the "quasi-equilibrium" properties of the resulting plasmoids. For this reason, in a series of calculations, a discrete number of background plasma temperatures (1, 5, 7, and 10 keV) were combined with a number of different magnetic field strengths (1, 2, 3, and 4 tesla). The results of these calculations are shown in Figs. 21 to 27. The rest of the pellet and plasma parameters used in these calculations are identical to those listed under "reference conditions" (see previous section).

Figure 21 shows the variation of the maximum plasmoid radius as a function of the plasma temperature for the magnetic field strengths listed. The times displayed on the curves correspond to the moments at which the maximum radius is reached. Note that the mass source is on until $\tau = 20\ \mu s$. Figure 22 is analogous to Fig. 21 but corresponds to the time at which the mass source is cut off.

As can be seen, at low and intermediate plasma temperatures ($T_e^\infty \simeq 5$ keV for the set of pellet and plasma parameters considered), the ionization time, and thus the starting moment of the interaction with the magnetic field, rapidly decreases with increasing incident heat flux. At the same time, the rate of pressure build-up is not sufficient to balance the $\vec{j} \times \vec{B}$ force (except at very low magnetic field strengths; see the curve $B_o = 1$ tesla), and the maximum attainable plasmoid radius continuously decreases with increasing plasma temperature. The stronger the magnetic field, the more pronounced is this effect. At higher energy input rates ($T_e^\infty \gtrsim 5$ keV) the pressure build-up is sufficient to prevent further radius reduction or even makes the plasmoid radius grow with ambient plasma temperature, in spite of the reduced ionization time. This effect is evident from the "quasi-steady" radius values displayed in Fig. 22. The variations both of the maximum attainable and of the "quasi-steady" plasmoid radii with the strength of the magnetic field applied are quite pronounced. The plasmoid radii displayed in Fig. 22 are somewhat smaller than those of Fig. 21: this is due to longitudinal expansion and m.f. rediffusion effects.

The bulk plasmoid density and the bulk plasmoid temperature prevailing at $\tau = 20\ \mu s$ are shown in Figs. 23 and 24, respectively, as functions of T_e^∞ and B_o. The dependence on the magnetic field strength (i.e. on the magnitude

of the stopping radius) is pronounced: the higher the m.f. strength and thus the smaller the plasmoid radius, the higher is the bulk plasmoid density and the lower is the bulk plasmoid temperature. The plasmoid density, just as the plasmoid radius, is a relatively weak function of the background plasma temperature. More pronounced is the heat flux dependence of the bulk plasmoid temperature.

The average magnetic field strength inside the plasmoid, B_{cld}, reduced by the applied field strength B_o,

$$B_{cld}/B_o = 2\pi \int_o^{R_{cld}} rB(r)dr/B_o A_\perp \ ,$$

is shown in Figs. 25 and 26 as a function of T_e^∞ and B_o for two different times: $\tau = \tau(R_{max})$ and $\tau = 20\ \mu s$, respectively.

The differences between these two figures are due to magnetic field rediffusion and to changes of the plasmoid cross-section during the frozen-in field expansion phase. As can be seen, the plasmoid becomes pronouncedly diamagnetic when subjected to higher heat fluxes (plasma temperatures), particularly at lower magnetic field strengths. The reason for such behavior is obvious: higher plasma temperatures means shorter ionization times at the plasma periphery; hence a frozen-in state is reached at an earlier time instant. Furthermore, lower applied magnetic field strengths allow further gasdynamic expansion during the frozen-in state. The last figure of this series, Fig. 27, shows the variation of the bulk ionization degree (defined analogously to the other bulk properties) prevailing at $\tau = \tau(R_{max})$, with T_e^∞ and B_o.

As can be seen, within the range of parameter values considered, the bulk ionization degree associated with $\tau = \tau(R_{max})$ varies from ~ 0.2 at $T_e^\infty = 1$ keV to ~ 0.5 at $T_e^\infty = 10$ keV and is only weakly dependent on the magnetic field strength applied. It is noteworthy that even at the highest plasma temperature considered, the cloud is only 50 % ionized when the radial expansion already comes to a full stop.

(e) Effect of the Number of Lagrangian Cells Used

In a few series of runs, the number of Lagrangian cells used in the numerical calculations was varied from 1 (single-cell approximation, see Ref. [12]) to up to 30. Representative results of such calculations are shown in Figs. 28 and 29 for the reference plasma and pellet conditions defined, and for a case with $r_p = 1$ mm and $T_e^\infty = 4.3$ keV (the other parameters being equal to those of the reference case). In these figures, the maximum plasmoid radius attained and the plasmoid radius reached after an expansion time of 20 μs (which is equal in this case to the cut-off moment of the mass source) are shown as functions

of the number of Lagrangian cells applied. As can be seen, the maximum and asymptotic values of the plasmoid radius (and of all quantities that are functions of the expansion rate) are rather sensitive functions of the mesh size (cell numbers) applied, particularly for a small number of Lagrangian cells. No significant changes can be observed for cell numbers $\simeq 30$. The effect of the mesh size is intimately coupled with the ionization dynamics computed: in the case of a coarse mesh the mass fraction contained in the outer cells is relatively large and it takes a longer time to ionize it. Hence the interaction with the magnetic field is delayed and the plasmoid gains a larger initial momentum in the transverse direction. The maximum value of the calculated plasmoid radius thus increases as the number of cells decreases. If one decreases the size (mass) of the cells at the periphery of the plasmoid, the first cell (being in direct contact with the ambient plasma) becomes ionized faster, the deceleration and stopping processes set in faster and the maximum plasmoid radius attained becomes smaller. The results of computations show that no significant variation in the computed plasmoid properties results if the number of Lagrangian cells is increased to over 30. To reduce computer time (CPU time) all calculations reported on here were performed with 20 Lagrangian cells. As can be seen from Figs. 28 and 29, the difference of the resulting plasmoid radii associated with these two cell number values is $\approx 5\%$ as compared with the 30-cell case. The variation of the associated plasma parameters is of the same order of magnitude.

Note that in the case of the single-cell approximation the plasmoid radius may increase monotonically during the first 20 μs (or even beyond this time) because of the relatively slow time increase of the respective bulk ionization degree (see Fig. 28). In a multi-cell approximation, the ionization (and thus the deceleration) of the peripheral cell may occur on a much shorter time scale. The times at which the maximum radius is reached (the first maximum, if Alfvén oscillations are present (see Fig. 29)) are displayed in Figs. 28 and 29.

Figure 30 shows the magnetic field reduction computed as a function of the mesh size for two different times: $\tau(R = R_{max})$ and $\tau = 20\ \mu s$. Note that B here is the magnetic field strength averaged over the cross-section of the plasmoid: $B = \int rB(r)dr / \int rdr$. The first curve demonstrates the effect of magnetic field expulsion (the finer the mesh, the earlier the frozen-in state is reached in the peripheral cell and the lower is the resulting B_{cld} value), the second one the reduction of the plasmoid cross-section and the m.f. rediffusion effect. Figures 31 and 32 display, for the same case ($r_p = 1$ mm, $T_e^{\infty} = 4.3$ keV) the variations of the computed cloud density and the cloud temperature as functions of the mesh coarseness. Again, two curves corresponding to different times $\tau = \tau(R = R_{max})$ and $\tau = 20\ \mu s$ are displayed. The difference between the two density curves is due to volumetric dilution, whereas the difference between

the two temperature curves is due to the heating of the cloud by the incident plasma electrons. The notably larger temperature increments associated with coarser mesh sizes is a result of the larger surface area ($\propto R_{max}^2$) exposed to the electron flux at lower total cell numbers.

The results clearly show that cloud radii computed by means of a single-cell approximation may be by a factor of $\simeq 2$ off those computed with allowance for the presence of radial structures in the cloud.

V. CONCLUSIONS

(a) Cloud evolution

Owing to the rapid pressure build-up in the cloud formed by the neutral particles released, the maximum expansion velocity of the neutral cloud for the plasma parameters and particle deposition rates investigated may reach several 10^4 m/s. It will be noted that this velocity is an order of magnitude higher than the typical pellet injection velocities applied in tokamaks. Shortly after the outer shell of the cloud becomes ionized, the cloud expansion comes to a stop in the direction perpendicular to the magnetic field. The stronger the magnetic field applied, the faster is the stoppping of the lateral cloud expansion. A diamagnetic cavity may be formed inside the cloud. Hence the radial dimension of the plasmoid produced is defined by the characteristic ionization time (i.e. the heat flux affecting the cloud and the ionization energy of the particles) and the magnetic field strength applied. For the range of plasma and particle source parameters considered, the characteristic ionization times and the resulting plasmoid radii are of the order of a few μs and a few mm, respectively. The length of the plasmoid is determined by the free expansion along the magnetic field lines and, if the maximum velocity of this free expansion is limited to the respective sonic velocity, the length of the plasmoid varies from a few cm at the time of completion of the ionization (end of the H_α radiation emission) to several tens or hundreds of meters at the time of full equilibration with the background plasma.

The evolution of the cloud is characterized by two different time scales:

(1) radial equilibrium ("quasi-steady" state) is reached on a time scale comparable to the Alfvén time scale (ratio of the plasmoid radius to the Alfvén velocity), which is measured in μs; (2) the axial expansion, rediffusion of the magnetic field, and equilibration with the background plasma occur on hydrodynamic and resistive diffusion time scales, which are measured in ms or tens of ms. The exact duration of this phase depends upon, besides the axial expansion rate, the radial diffusion processes as well. The calculated plasmoid radii as

well as the length-to-diameter ratios characterizing the unionized portion of the cloud (at the moment of reaching the maximum radius) are in good agreement with experimentally observed values.

(b) Cloud structure

The radial heat flux affecting the cloud surface that expands across the magnetic field lines induces a thermal wave that propagates in the interior of the cloud. The resulting nonuniform radial distributions of the temperature, electron density, and $\vec{j} \times \vec{B}$ force lead to a characteristic cloud structure with a lifetime extending into the hydrodynamic expansion phase. The major characteristics of the resulting radial structures are as follows:

(b.1) Hollow temperature profile with only a few eV in the plasmoid interior. The temperature of the peripheral plasmoid layers is two orders of magnitude higher. The experimental (anomalously high) thermal diffusion coefficients used in these computations yield thermal equilibrium times measurable on the hydrodynamic time scale.

(b.2) Centrally peaked particle density profiles during the entire evolution time (both the Alfvén and the hydrodynamic expansion phases). Hence, owing to the possibility of particle escape along the magnetic field lines, there is no notable pile-up of the ions at the ionization radius. The lifetime of the density inhomogeneities is measured on the hydrodynamic time scale, and, if coupled to negligible particle diffusion in the radial direction, it may be rather long (the lifetime of 'snakes' observed in pellet-fueled JET discharges [35] was of the order of 2 s).

(b.3) The electron density profile simulated is first hollow (like the temperature profile) and then, upon completion of the ionization process, it becomes identical with the particle density profile and remains centrally peaked for the rest of the expansion time. Typical maximum electron densities calculated are of the order of $10^{24}\ m^{-3}$, i.e. four orders of magnitude larger than the backgound electron density. It is of interest to compare here the calculated cloud temperatures (cloud interior) and electron densities (maxima) with measured values. The following cloud characteristics ($n_{e_{max}}$ and $T_{e_{min}}$) are reported in the literature:

PLT [21]	2.4×10^{23} to $10^{24}\ m^{-3}$ / 2 eV;
TEXT [23]	$6 \times 10^{23}\ m^{-3}$ / 2.5 eV;
TFTR [24]	$6 \times 10^{23}\ m^{-3}$;
TFR [22]	$1.2 \times 10^{23}\ m^{-3}$ / 1.5 eV;
ISX-B[36]	$10^{24}\ m^{-3}$.

The correspondence between the calculated and measured values is obvious.

(b.4) The magnetic field distribution inside the cloud is defined by the evolution of the electrical conductivity structure: as soon as the outer cloud shell becomes ionized, the magnetic flux enclosed is practically frozen in, and the magnetic field topology is primarly determined by the variation of the cloud radius. The strength of the magnetic cavity produced (i.e. the reduction of the $\langle B \rangle / B_o$ ratio) may be substantial. Since the energy flux carried by the thermal plasma electrons along the field lines to the cloud is a function of this ratio (a function of the number of field lines piercing the cloud), the **magnetic shielding** thus produced may be significant and should not be neglected in up-to-date ablation calculations.

(b.5) The present calculations show that the characteristic dimension of the radial structures is defined by the ionization radius and the magnetic field strength. The question may arise whether the radial structures computed here are related to the striations observed in the pellet wakes in tokamak plasmas. Since the present calculations are based on a stationary mass source approximation, no conclusive answer can be given. However, the time-resolved measurements of Durst [25], - see Figures 4.8, 4.9 and particularly 4.10 [25], which gives a sequence of framing camera pictures, each with an exposure time of 0.2 μs and a delay of 1 μs between the succesive pictures - show that the velocity of the pellet traversing its own cloud has little influence, if any, on the cloud structure as long as the pellet resides within the ionization radius. Hence, the striated wake observed in various tokamaks may be related to a pattern produced by a sequence of structures such as those calculated here, with the local ionization radius as the characteristic distance (wavelength) separating them. Obviously, the proper way to prove this hypothesis would be to calculate the cloud structure caused by a moving mass source, a task that is beyond the scope of the present work.

(c) Mass deposition rate, plasma temperature, and magnetic field effects

The time necessary for ionization of the outer plasmoid shells is a function of the balance between the deposition rate of the cold particles and the heat flux available for heating and ionizing these particles. On the other hand, the confinement radius of the plasmoid layers is defined by the balance between the pressure build-up (pressure gradients) and the retarding $\vec{j} \times \vec{B}$ forces, both of which are again functions of the energy input rate (the latter through the electrical conductivity). In addition, the retarding force is also a function of the magnetic field strength and its distribution as well. The results of calculations show that the "quasi-steady" plasmoid properties are complex functions of all these parameters combined. No simple analytical (or ad hoc) description of

this functionality, as is done in present ablation models, where the size and state parameters of the shielding cloud are approximated, seems to be possible. Up-to-date predictive ablation codes should incorporate computation of these characteristics.

(d) Limitations of the present work

(d.1) The present work, even with a stationary particle source being assumed, approximates an inherently two-dimensional process by a one-dimensional model. In particular, the particle stopping lengths, temperature and density gradients, and magnetic field variation (mirror-like field topology) existing along the field lines have been disregarded. No intermixing of the nested annular cells was allowed . However, intermixing of annular fluid layers is reduced to a minimum, if not canceled, as soon as these layers become ionized and attached to magnetic flux surfaces. The ionized fluid expands preferentially along the magnetic field lines, whether or not the two-dimensionality of the expansion is taken into account. Furthermore, the initial expansion of the cold neutral cloud and that of the residual neutral cloud core region at later times remain (practically) spherically symmetric in the present approximation as well. Hence, the logical error is limited to the expansion phase of those Lagragian cells that are already captured by the radial heat wave but are not yet ionized. Fortunately, this is a relatively short phase of the expansion. Important is the fact that the global energy transport to the cloud by the thermal plasma electrons in the direction parallel to the magnetic field lines is correctly modeled (although the finite stopping lengths and all other gradient effects along the magnetic field lines are neglected), and that the density and temperature changes in the Lagragian cells which are associated with the axial expansion of these cells are taken into account when the dynamics of the radial expansion and magnetic confinement of these cells are calculated.

The primary objective of this work was to obtain information on the radial expansion dynamics and the resulting structures in high-density particle clouds expanding in magnetically confined plasmas. The agreement with experimental results shows that the present $1\frac{1}{2}$-D approximation is realistic.

(d.2) A single-temperature, single-velocity approximation is used throughout the present work. The single-temperature approximation is justified by the high collisionality of the plasmoid during the entire evolution period considered. The single-velocity approximation is valid both for the initial neutral gas expansion and for the fully ionized plasmoid expansion phases, but it certainly needs justification for the transition between the two phases listed when a partially ionized gas consisting of ions, electrons, and neutrals expands in a magnetic field. Calculations performed with a quasi-two-velocity single-cell La-

grangian model [37] yielded results comparable to those of the single-velocity approximation. In these calculations the ions were assumed to be captured instantaneously ($v_\perp = 0$) at the magnetic surfaces where they were born and the momentum transfer among the fluid components was calculated by accounting for the respective friction forces. Hence, in view of the difficulties associated with the description of multi-component fluids in Lagragian systems, it was decided to use here a single-velocity approximation.

(d.3) The stability analysis of the plasmoid configuration obtained has been omitted. Obviously, the high-density plasmoid radially decelerating in a magnetically confined low-density plasma is subject to the MHD version of the classical Rayleigh-Taylor instability, i.e. to flute instability. Indeed, earlier investigations performed in the single-cell Lagrangian approximation [20a] showed that in a certain expansion phase the wavelength of the flutes expected becomes of the order of the plasmoid radius; this may be another explanation for the striations seen in pellet wakes. Another instability that can affect the plasmoid in a curved or toroidal magnetic field is the polarization-induced high-β drift instability [38]. The characteristic drift velocity is given in this case by the ion acoustic velocity. Hence plasmoids with temperatures of the order of 10 eV would be lost to the torus wall within a few μs. Since such violent particle loss has not been observed in pellet-fueled tokamaks, it is most likely that the plasmoid polarization is drastically reduced or canceled by equilibrating return currents whose paths are closed through the background plasmas in pellet-fueled tokamaks.

REFERENCES

(1) C. T. Chang, L.W. Jorgensen, P. Nielsen, L. L. Lengyel, Review Paper: "The Feasibility of Pellet Refueling of a Fusion Reactor". Nucl. Fusion **20** (1980) 859.

(2) S. L. Milora, "Review of Pellet Fueling". J. Fusion Energy **1** (1981) 15.

(3) M. Greenwald et al., "Energy Confinement of High-Density Pellet-Fueled Plasmas in the Alcator - C Tokamak". Phys. Rev. Lett. **53** (1984) 352.

(4) G. L. Schmidt, S. L. Milora, and the TFTR Team, "Heating of Peaked Density Profiles Produced by Pellet Injection in JET". Plasma Phys. and Contr. Nucl. Fus. Res., Proc. of the 12th IAEA Conf., Nice, 1988, Vol. **1**, 215.

(5) M. Kaufmann et al., "Pellet Injection with Improved Confinement in ASDEX". Nucl. Fusion **28** (1988) 827.

(6) M. C. Zarnstorff et al., "Transport in TFTR Supershots". Plasma Phys. and Contr. Nucl. Fus. Res., Proc. of the 12th IEAE Conf., Nice, 1988, Vol. **1**, 185.

(7) D. P. Schissel, "Pellet Injection Experiments on DOUBLET-III". Proc.

International Pellet Workshop, La Jolla, Calif. Oct./Nov. 1985

(8) L. L. Lengyel, "Ignition and Fueling Scenario Calculations for Neutral-Beam-Heated Tokamak Reactors Based on Pellet Injection". Fus. Technology, **10** (1986) 354.

(9) Proc. IAEA Techn. Comm. Meeting on Pellet Injection and Toroidal Confinement,Gut Ising, FRG, 1988 (to appear); or see L. L. Lengyel, Conf. Rept. Gut Ising, Nuc. Fusion **29** (1989) 325.

(10) F. Engelmann "Prospectives of Pellet Injection in NET-Like Devices". Comments on Pl. Phys. and Contr. Fusion, Vol. XII, No 6 (1989) 293.

(11) P. B. Parks, R. J. Turnbull, and C. A. Foster, "A Model for the Ablation Rate of a Hydrogen Pellet in a Plasma". Nucl. Fusion **17** (1977) 539.

(12) S. L. Milora, and C. A. Foster, "A Revised Neutral Gas Shielding Model for Pellet-Plasma Interactions". IEEE Trans. Plasma Sci. **6** (1978) 578.

(13) P. B. Parks, and R. J. Turnbull, "Effect of the Transonic Flow in the Ablation Cloud on the Lifetime of a Solid Hydrogen Pellet in a Plasma". Phys. Fluids **21** (1978) 1735.

(14) M. Kaufmann, K. Lackner, L. L. Lengyel, and W. Schneider, "Plasma Shielding of Hydrogen Pellets". Nucl. Fusion **26** (1986) 171.

(15) W. A. Houlberg, S. L. Milora, and S. E. Attenberger, "Neutral and Plasma Shielding Model for Pellet Ablation". Nucl. Fusion **28** (1988) 595.

(16) L. L. Lengyel, "Pellet Ablation in Hot Plasmas and the Problem of Magnetic Shielding". Phys. Fluids **21** (1978) 1945.

(17) P. B. Parks, "Magnetic Field Distortion near an Ablating Hydrogen Pellet". Nucl. Fusion **20** (1980) 311.

(18) B. V. Kuteev, A. P. Umov, and L. D. Tsendin, "Two Dimensional Kinetic Model for the Evaporation of Hydrogen Pellets in Tokamaks". Sov. J. Plasma Phys. **11** (1985) 236.

(19) G. Zavala, T. Kammash, "Non-Spherical Pellet Ablation in Tokamak Plasma", Fus. Technology, **6** (1984) 30; see also: "Magnetic Field Effects on Pellet Ablation in Fusion Plasmas", Bull.Am.Phys.Soc. **28** (1983) 1151.

(20) L. L. Lengyel, (a) "Expansion of Dense Particle Clouds in Magnetically Confined Plasmas", Phys. Fluids **31** (1988) 1577,
(b) "Pellet-Plasma interaction: Local Disturbances Caused by Pellet Ablation in Tokamaks", Nucl. Fusion **29** (1989) 37.

(21) D. H. McNeill, G. J. Greene, and D. D. Schuresko, "Parameters of the Luminous Region Surrounding Deuterium Pellets in the Princeton Large Torus Tokamak". Phys. Rev. Lett. **55** (1985) 1398.

(22) TFR Group, "Deuterium Pellet Injection into Plasmas of the Fontenay-aux-Roses Tokamak TFR: Photographic and Spectroscopic Measurements of the Ablation Zone". Europhys. Lett. **2** (1986) 267.

(23) R. D. Durst, W. L. Rowan, et al., "Observations of Pellet Ablation Dynamics on TEXT". Bull. Am. Phys. Soc. **32** (1987) 1841.

(24) D. H. McNeill, D. K. Owens, G. L. Schmidt, "The Behaviour of Ablating Pellets in TFTR". Bull. Am. Phys. Soc. **32** (1987) 1926.

(25) R. D. Durst, "An Experimental investigation of the Dynamics of Pellet Ablation on the Texas Experimental Tokamak".
Ph. D. Thesis, The University of Texas, Austin, Texas, 1988.

(26) S. Valkealahti, J. Schou, and H. Sorensen,
"Ranges and Stopping Power of keV Electrons in Solid Hydrogen".
Nucl. Instr. and Methods in Phys. Res., **B34** (1988), 321.

(27) S. B. Mende, "Morphology of the Magnetospheric Barium Release".
J. Geophys. Res. **78** (1973) 5751.

(28) A. Gondhalekar et al., "Correlation of Heat and Particle Transport in JET Plasmas". Proc. IAEA Techn. Comm. Meeting on Pellet Ablation and Toroidal Confinement, Gut Ising, FRG, 1989.

(29) E. Hinnov, J. G. Hirschberg, "Electron-Ion Recombination in Dense Plasmas". Phys. Rev. **125** (1962) 795.

(30) Y. B. Zel'dovich, and Y. P. Raiser Physics of Shock Waves and High-Temperature Hydrodynamic Phenomena. Academic Press, N.Y., 1967.

(31) L. Spitzer, Physics of Fully Ionized Gases.
Interscience Publishers Inc., N.Y.. 1956.

(32) J. von Neumann, and R. D. Richtmyer "A Method for the Numerical Calculation of Hydrodynamic Shocks". J. Appl, Phys. **21** (1950) 232,
see also: R. D. Richtmyer and K. W. Morton, Difference Methods for Initial-Value Problems. Interscience Publishers Inc., N.Y., 1967.

(33) G. A. Wurden et al., "Pellet Ablation in the Reversed Field Pinch and Tokamak: a Comparison". Proc. 16th Europ. Cof. on Contr. Fus. and Pl. Phys., Venice, **13 B** (1989) Pt. IV 1561.

(34) A. Weller et al., "Density Perturbations at Rational q-Surfaces Following Pellet Injection in JET". in Contr. Fus. and Pl. Phys. (Proc. 14^{th} Eur. Conf. of EPS, Madrid, 1987) Vol. 11D, Part I, **25**.

(35) C.E. Thomas "An experimental Investigation of Solid Hydrogen Pellet Ablation in High-Temperature Plasmas using Holographic Interferometry and other Diagnostics". Rep. ORNL/TM-7468, (1981).

(36) L. L. Lengyel (to be published)

(37) A. Schlüter, Inst. f. Plasmaphysik, Garching, Rept. No 6/38 (1965);
see also: L. L. Lengyel, "Expansion of Laser Produced Plasmas in Stellarator Fields".
Nucl. Fusion **17** (1977) 805.

FIGURES

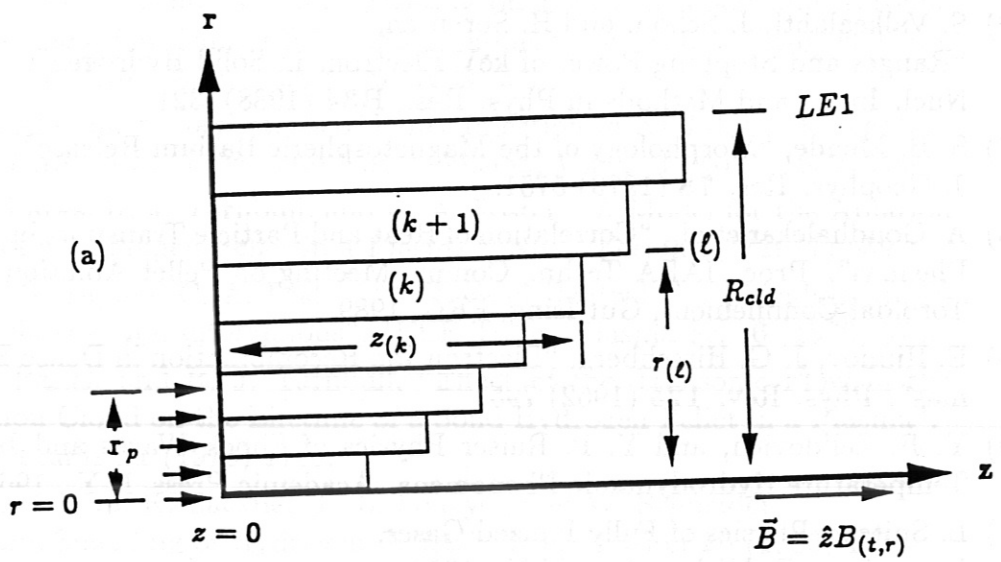

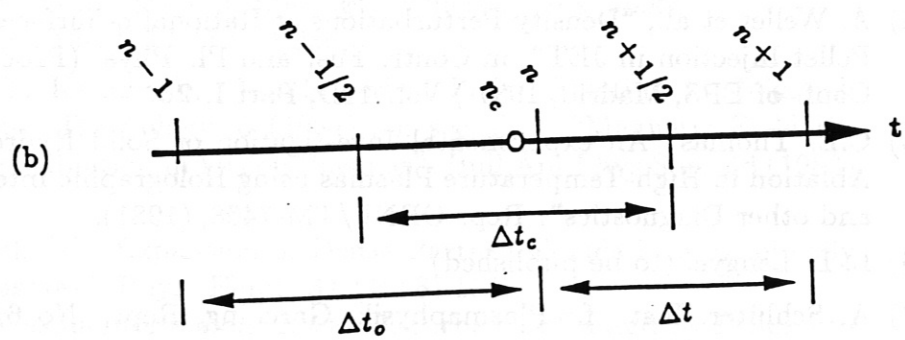

Fig. 1 The coordinate system considered:
(a) the Lagrangian mesh system,
(b) time centering scheme.

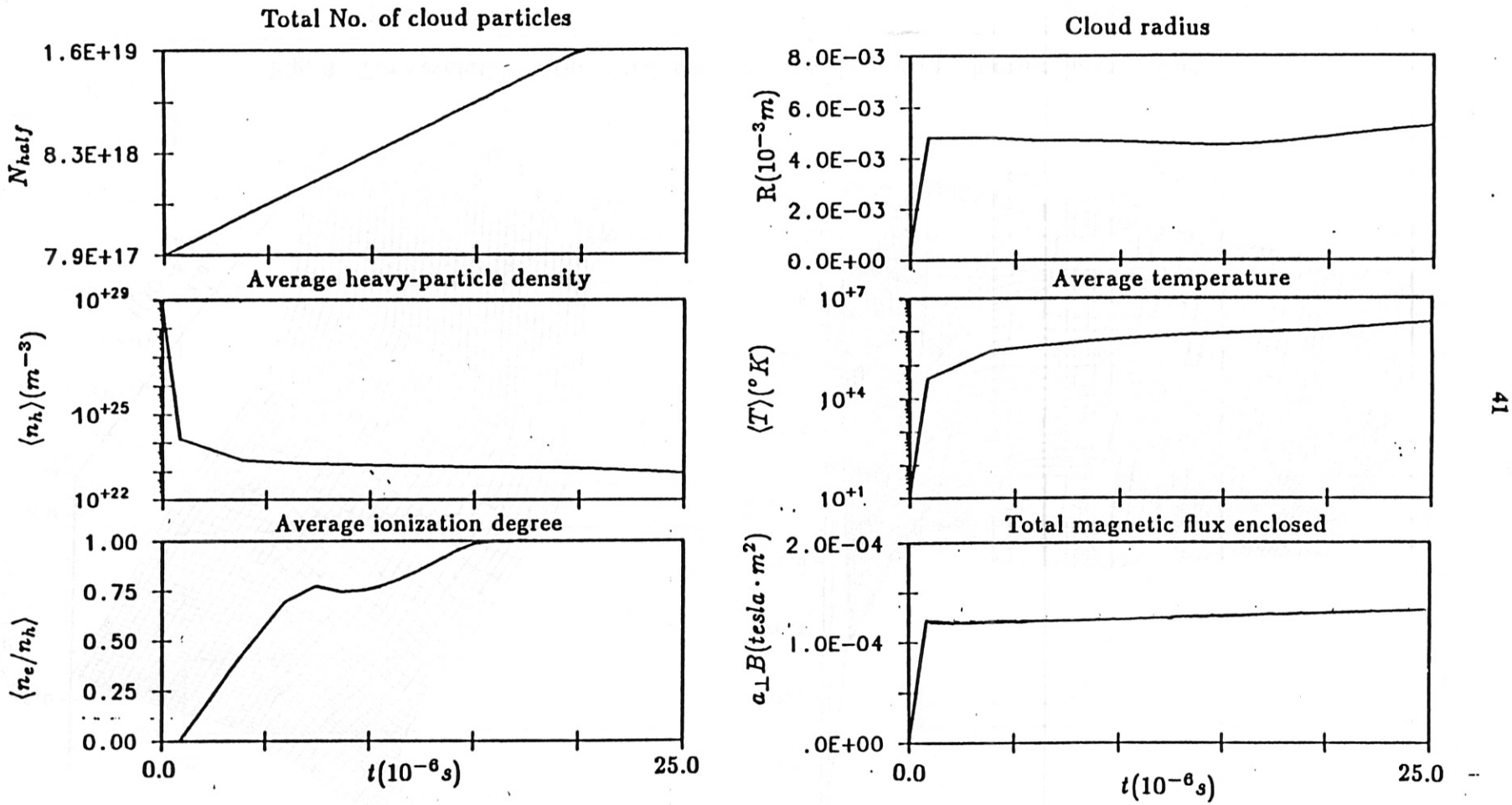

Fig. 2 Time variation of representative cloud parameters for the first 25 μs.

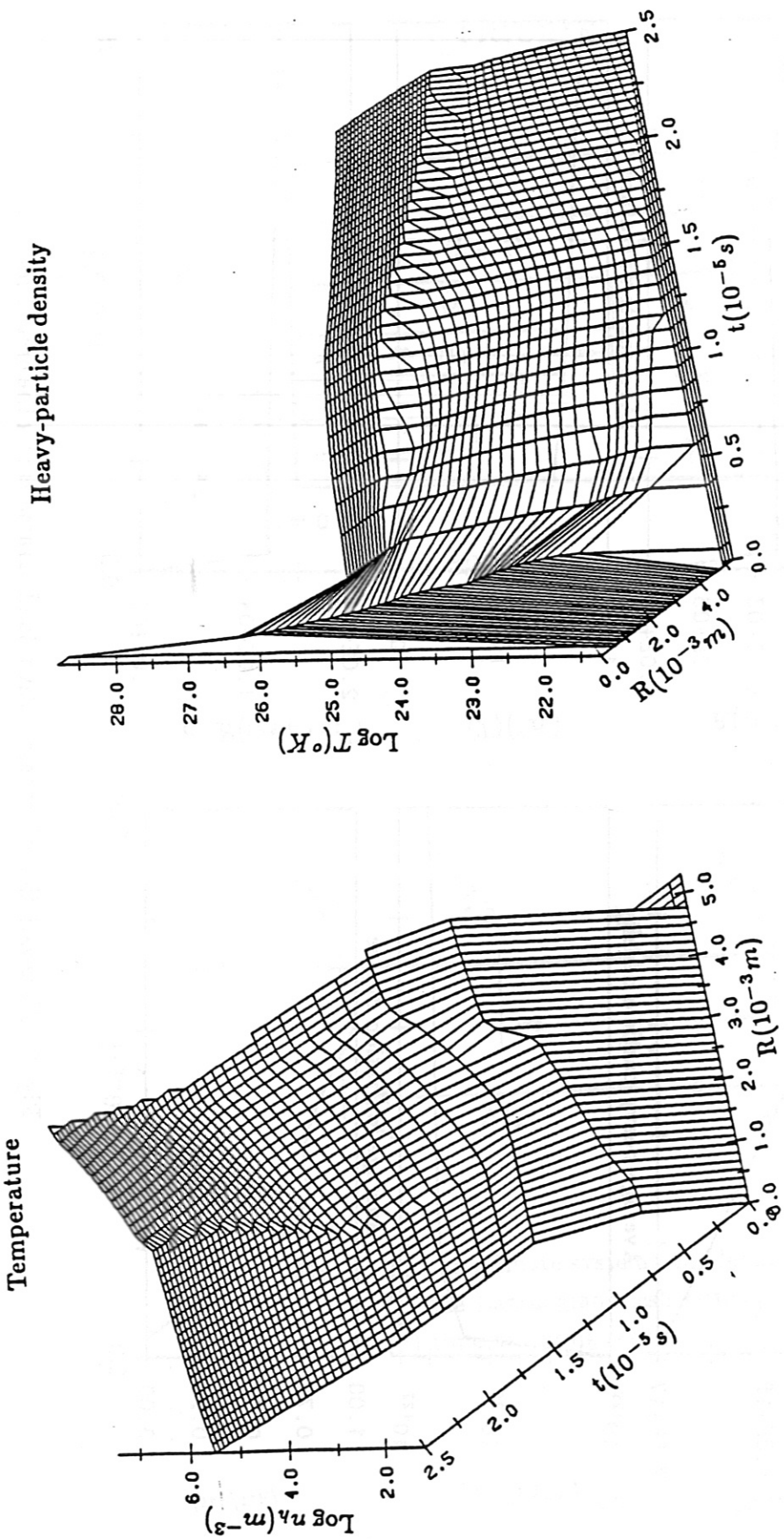

Fig. 3 Time evolution of the radial temperature and density profiles for the first 25 μs.

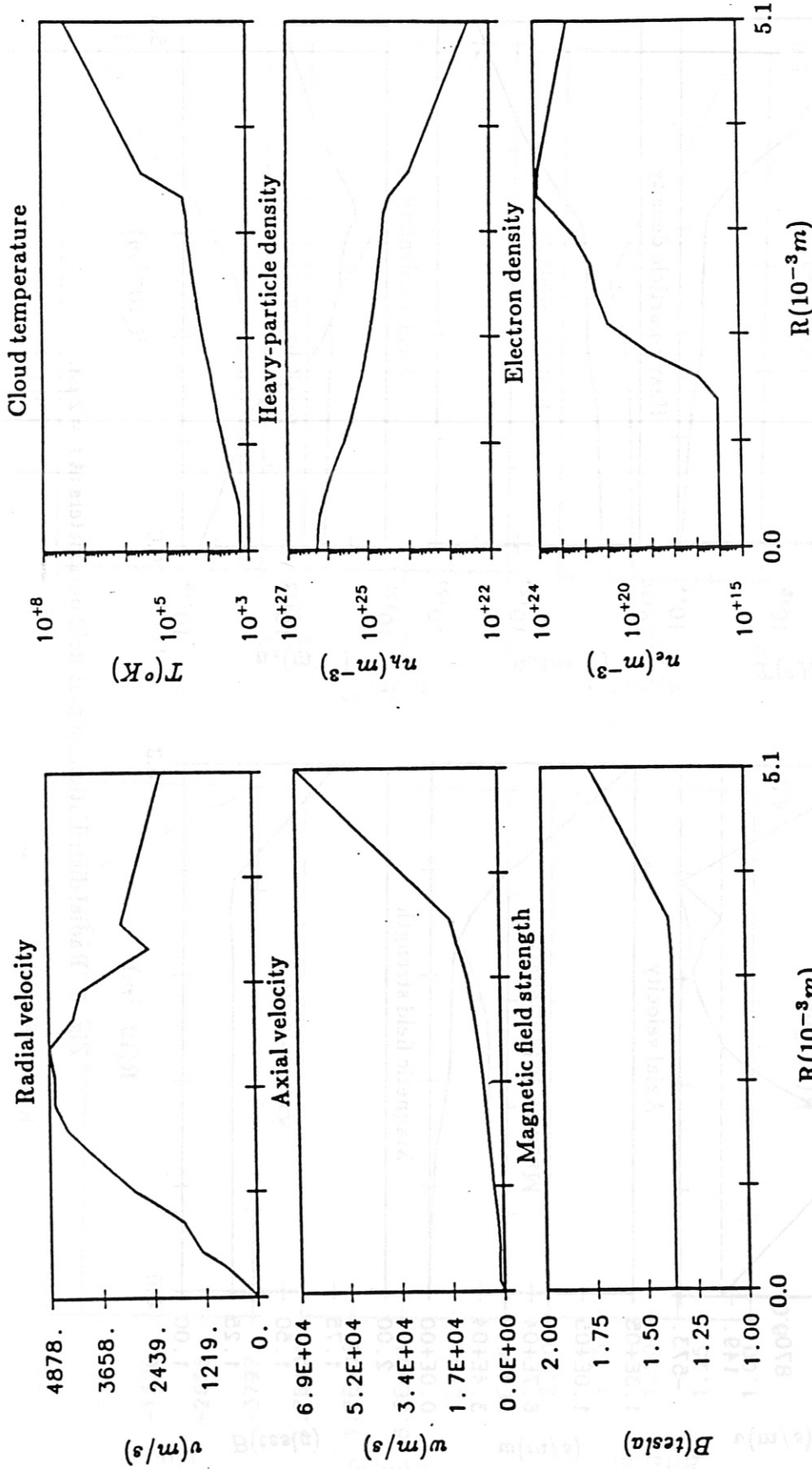

Fig. 4 Radial distributions of plasmoid parameters at $t = 1\ \mu s$.

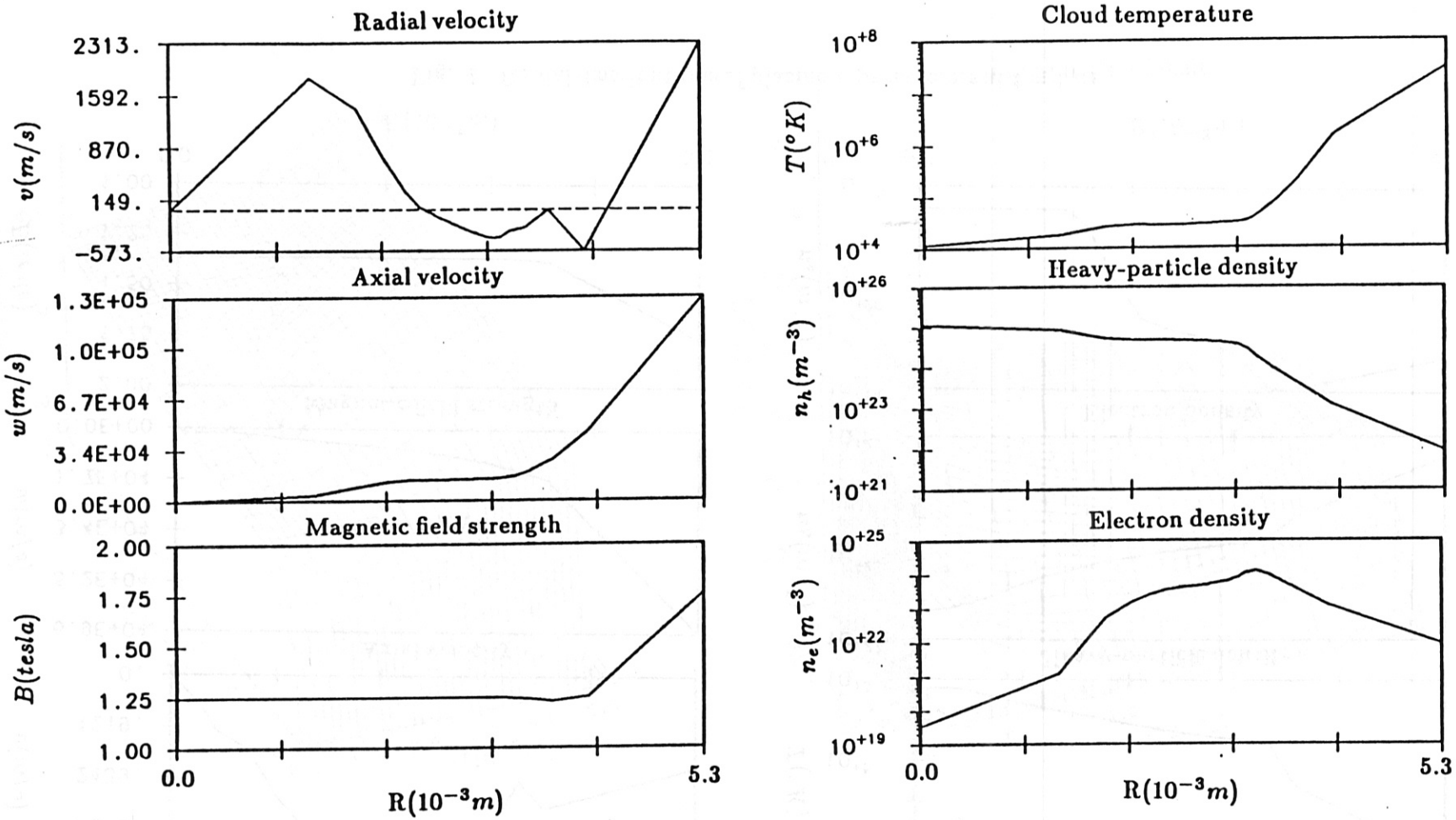

Fig. 5 Radial distributions of plasmoid parameters at $t = 2\ \mu s$.

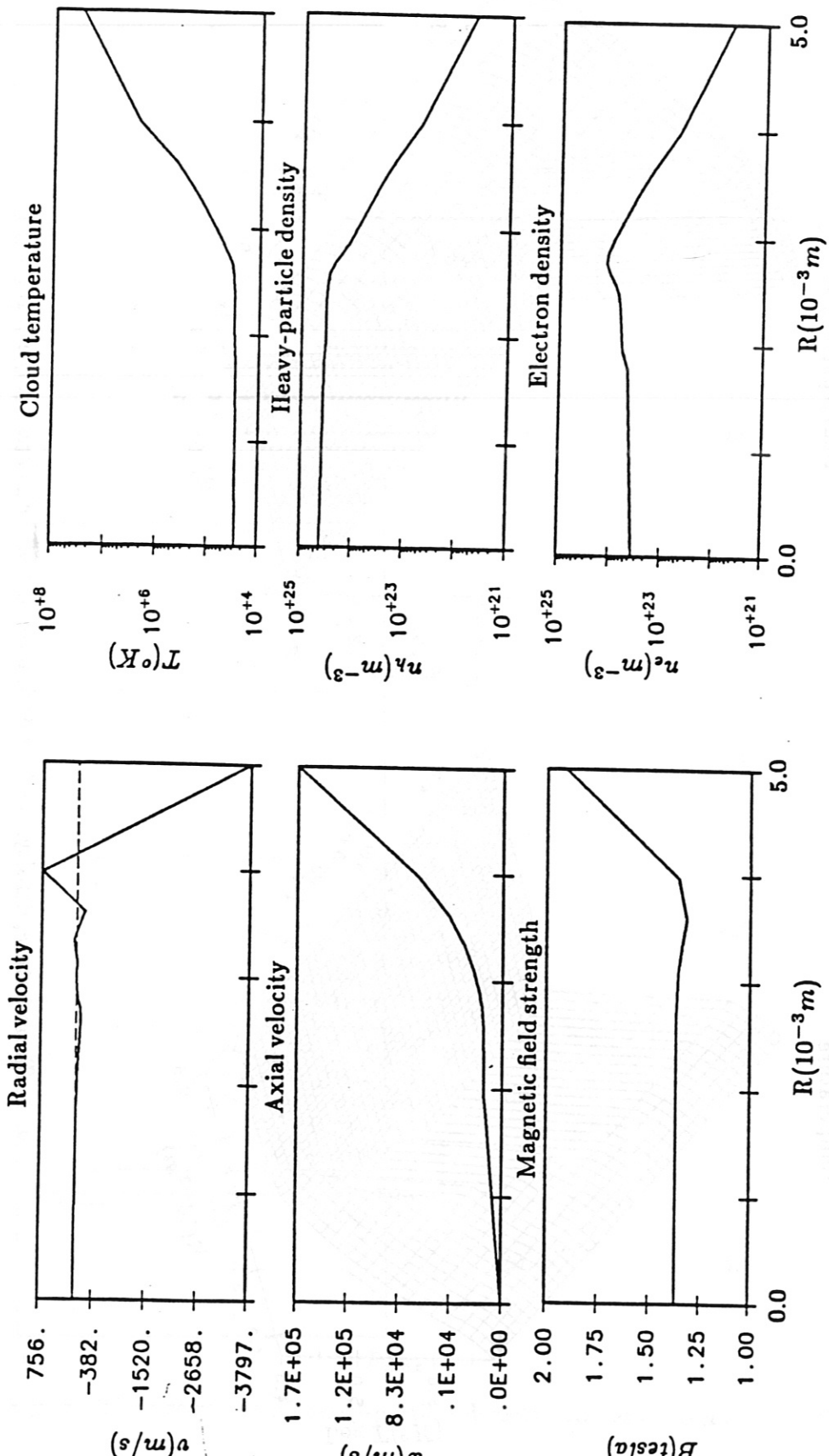

Fig. 6 Radial distributions of plasmoid parameters at $t = 3\ \mu s$.

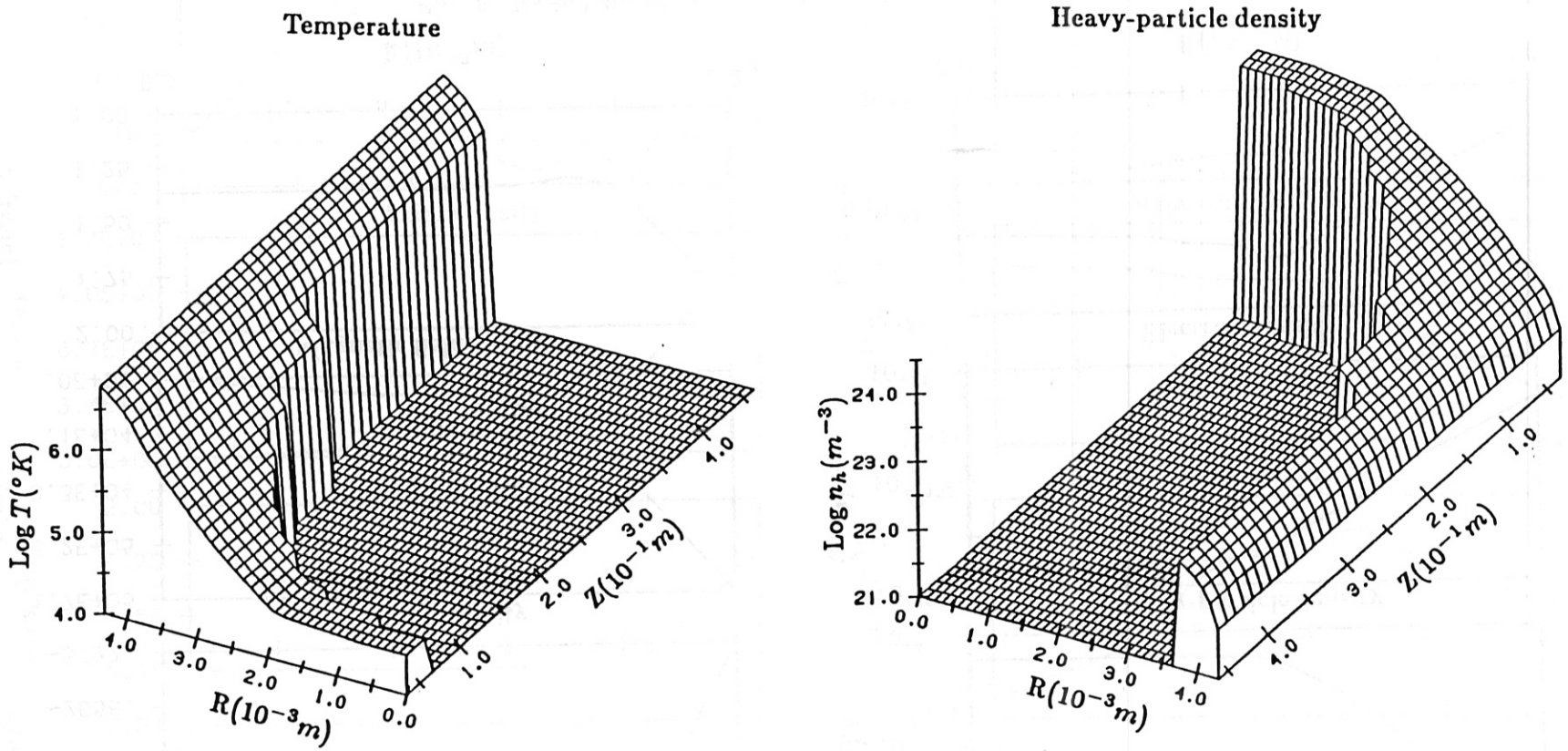

Fig. 7 Temperature, density, and longitudinal extent of the Lagrangian cells at $t = 5\ \mu s$.

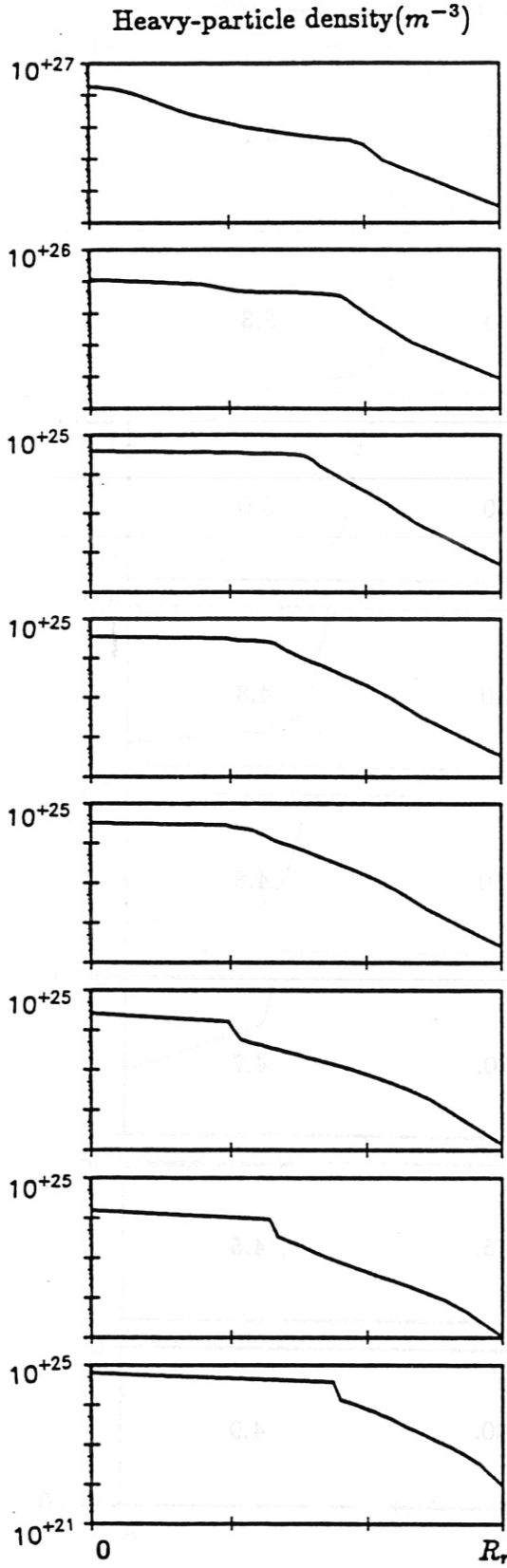

Fig. 8 Time sequence of heavy-particle density profiles for $0\ \mu s < t \leq 20\ \mu s$.

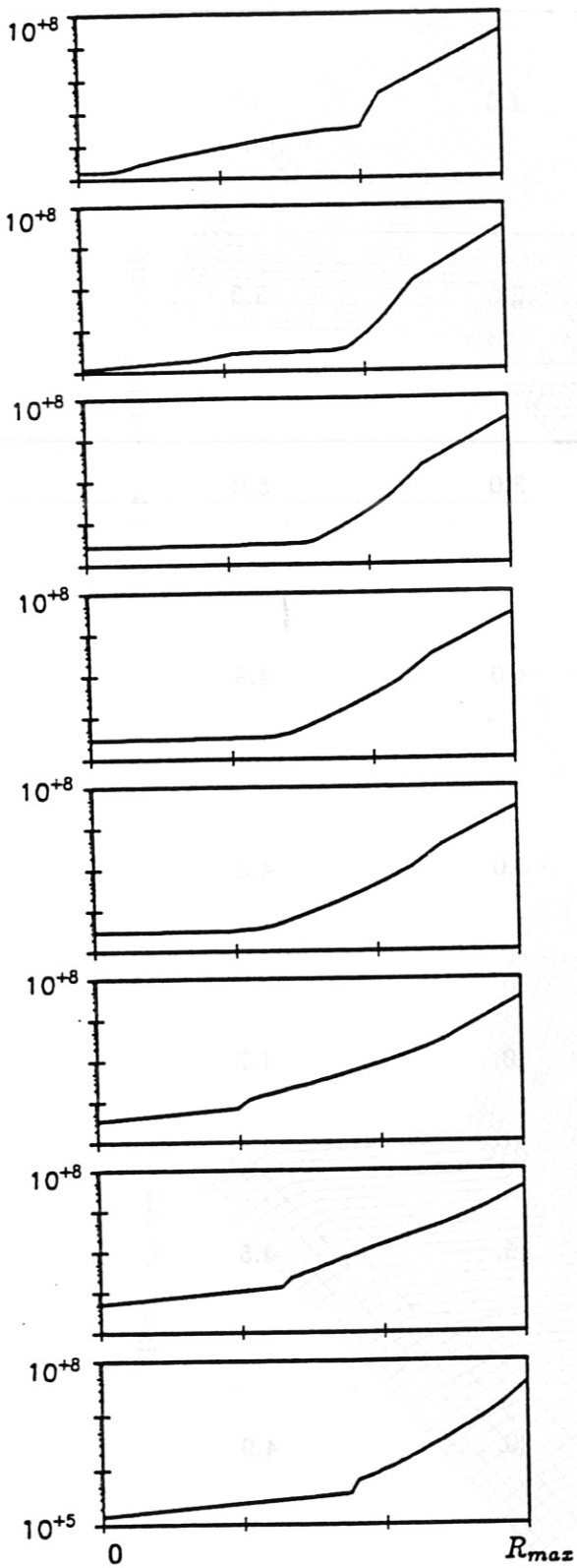

Time(μs)	$R_{max}(mm)$
1.0	5.1
2.0	5.3
3.0	5.0
4.0	4.8
5.0	4.8
10.	4.7
15.	4.5
20.	4.9

Fig. 9 Time sequence of cloud temperature profiles for $0\ \mu s < t \leq 20\ \mu s$.

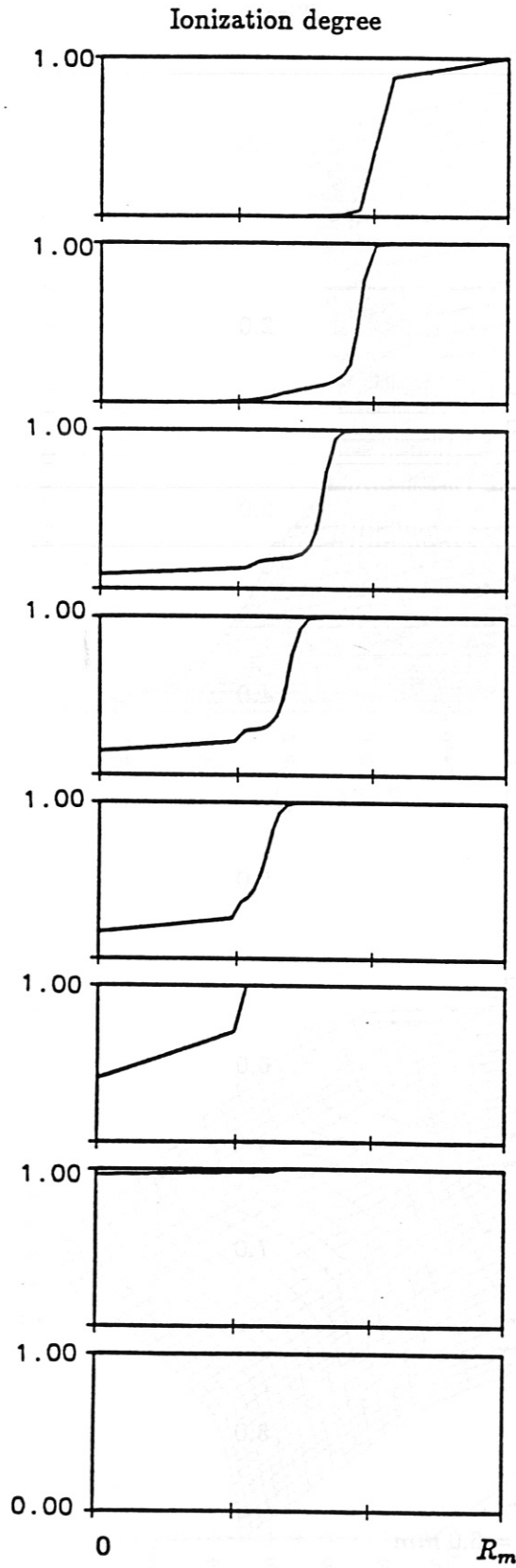

Time(μs)	$R_{max}(mm)$
1.0	5.1
2.0	5.3
3.0	5.0
4.0	4.8
5.0	4.8
10.	4.7
15.	4.5
20.	4.9

Fig. 10 Time sequence of ionization degree profiles for $0\ \mu s < t \leq 20\ \mu s$.

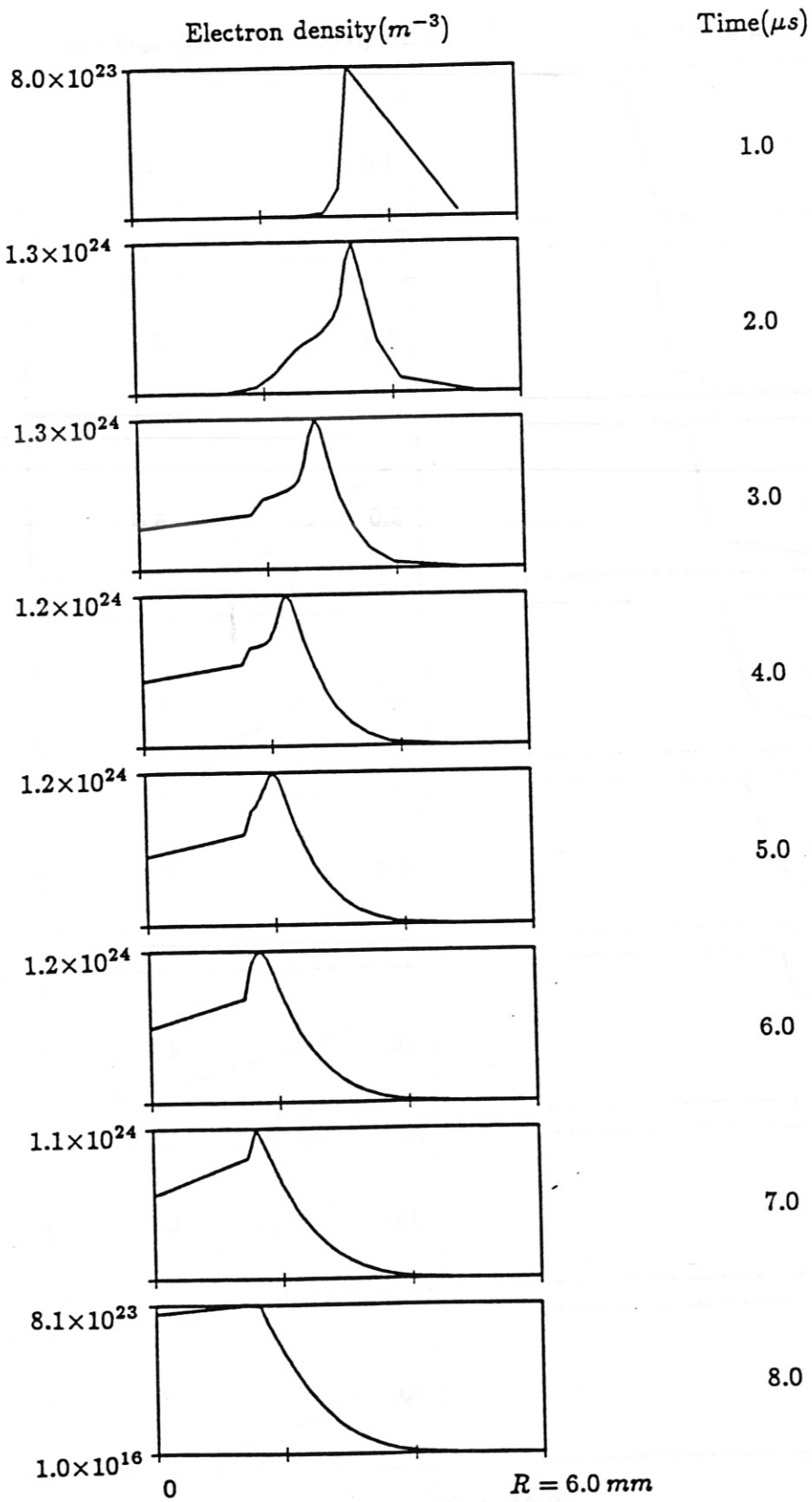

Fig. 11 Time sequence of electron density profiles for $0\ \mu s < t \leq 8\ \mu s$.

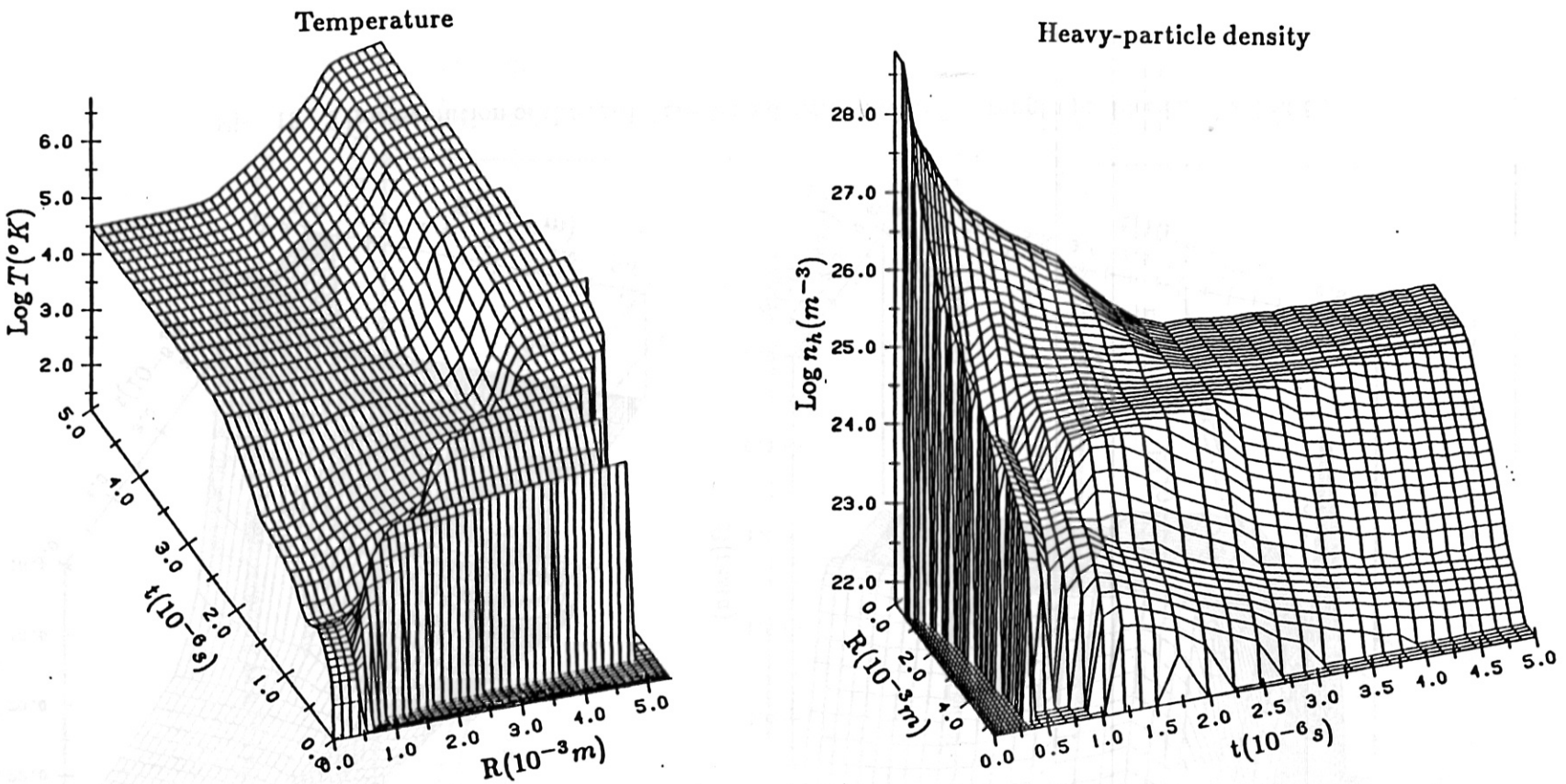

Fig. 12 Time evolution of the radial temperature and density profiles for the first 5 μs.

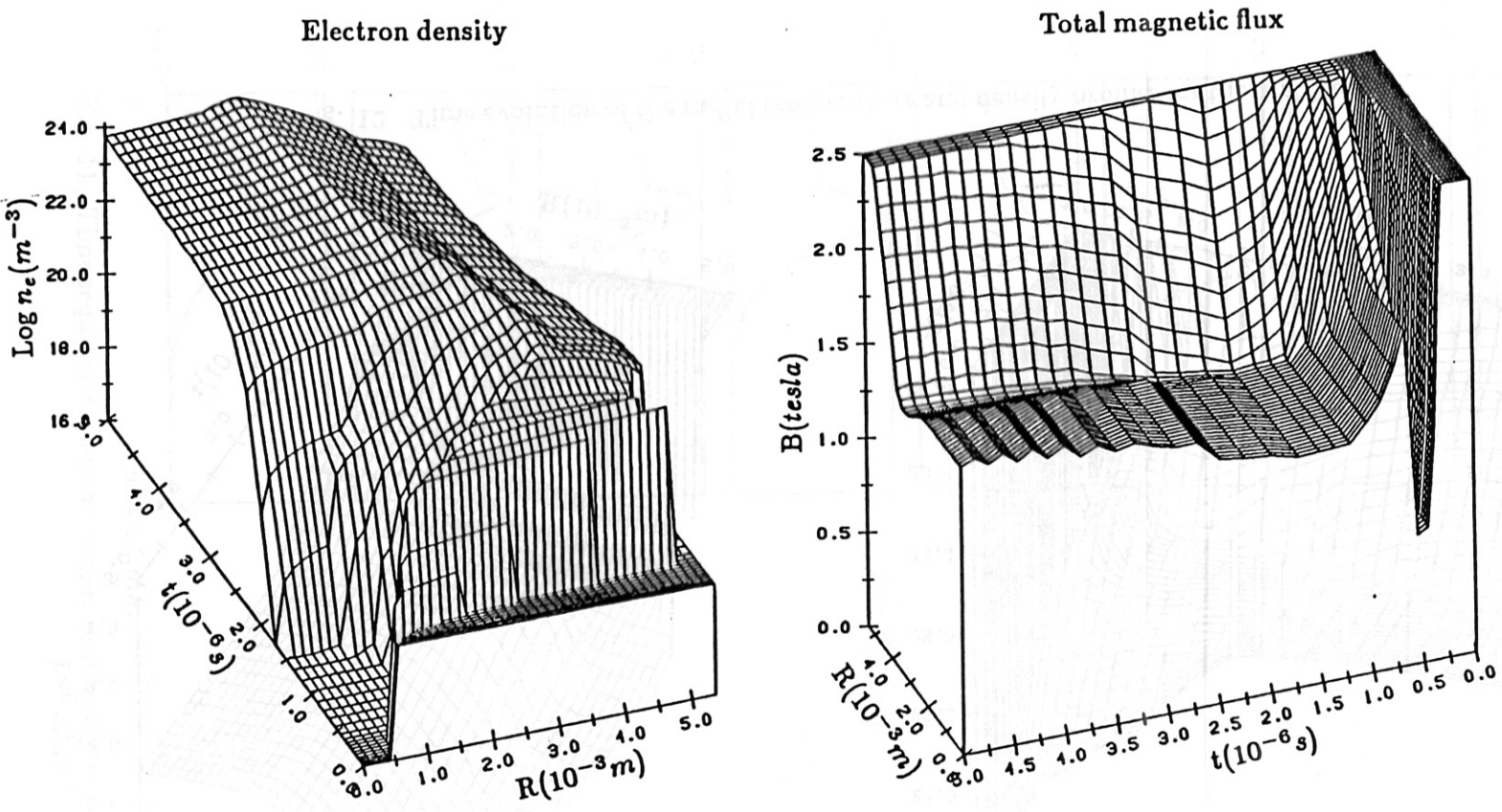

Fig. 13 Time evolution of the radial electron density and m.f. strength profiles for the first 5 μs.

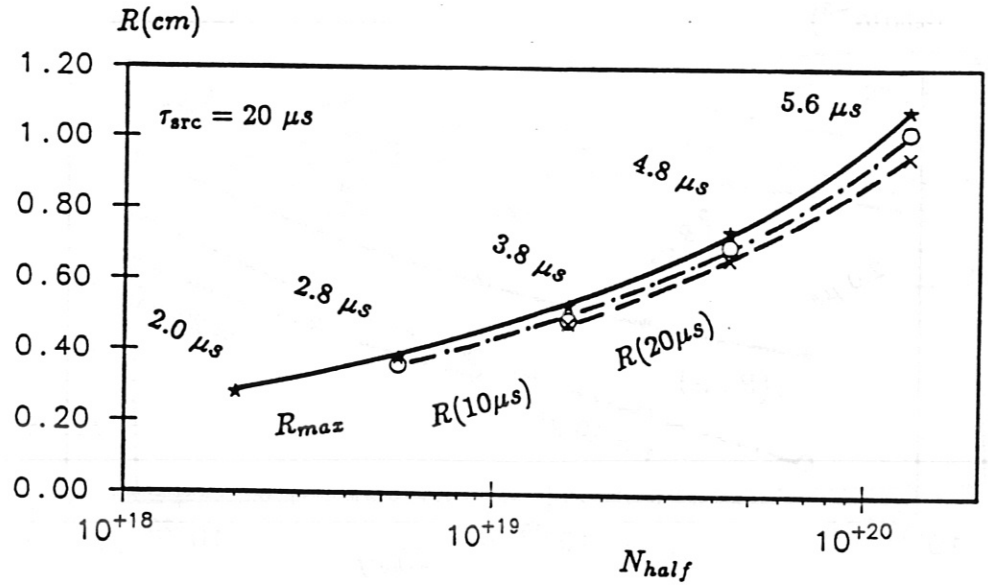

Fig. 14 Effect of the number of particles deposited within $\tau = 20\ \mu s$ on the plasmoid radius.

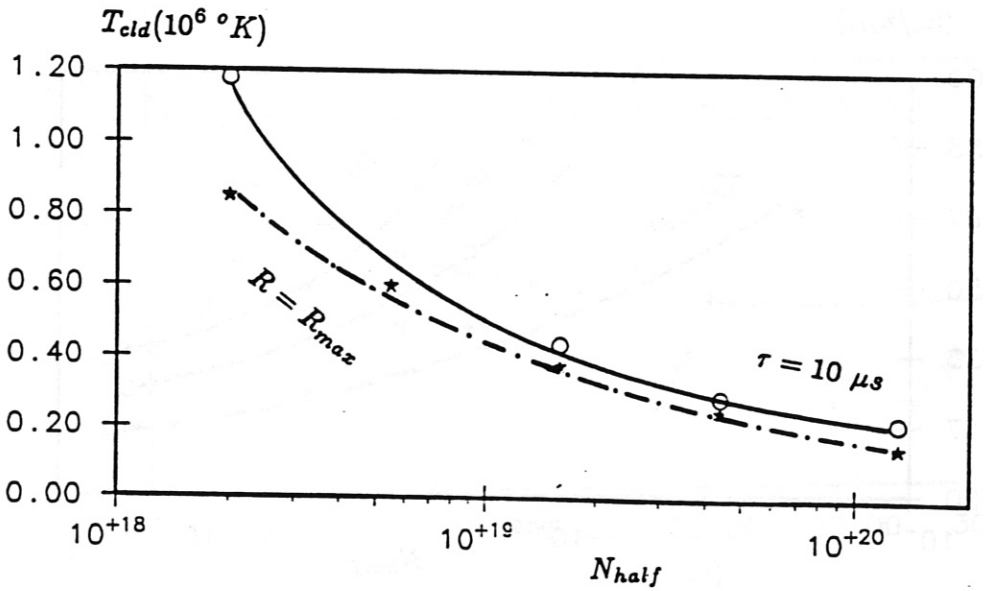

Fig. 15 Mass-averaged cloud temperature as a function of the number of particles deposited.

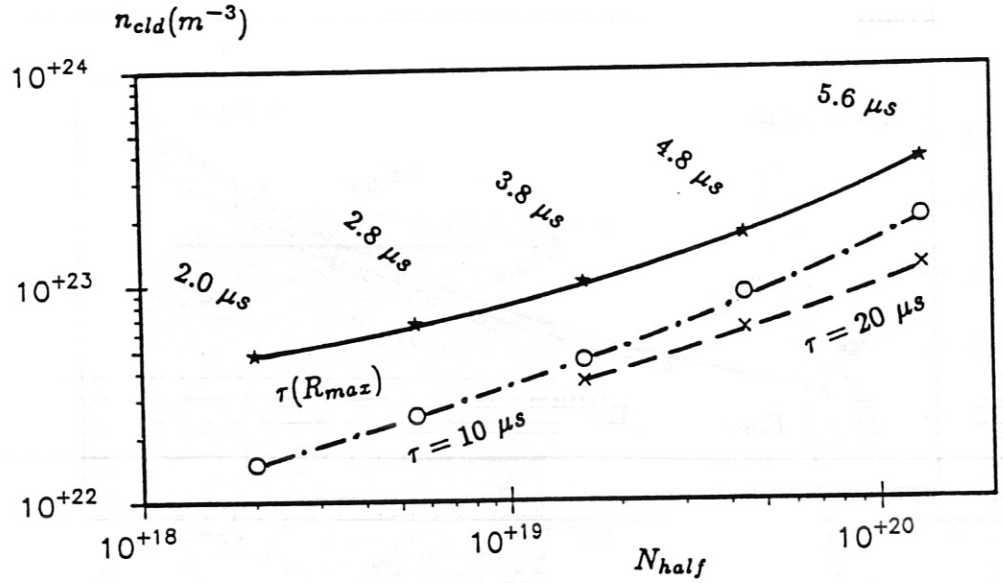

Fig. 16 Cloud density averaged over the volume as a function of the number of particles deposited.

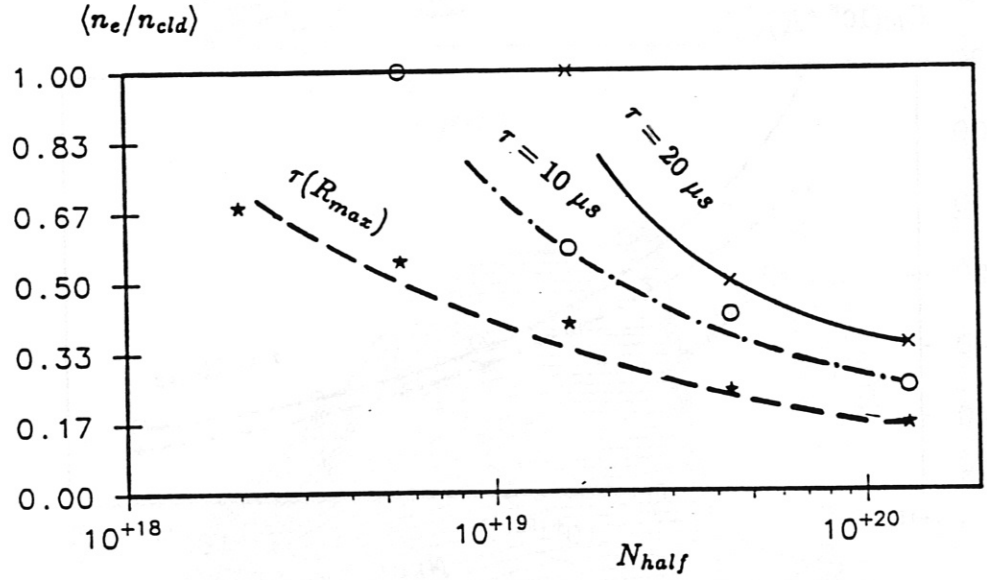

Fig. 17 Bulk ionization degree as a function of the number of particles deposited.

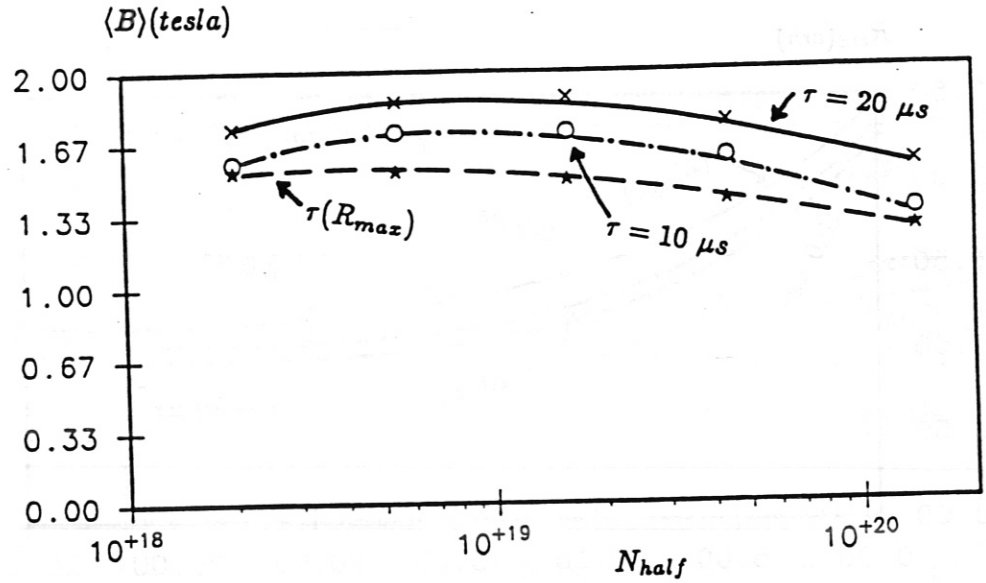

Fig. 18 Volume-averaged magnetic field as a function of the number of particles deposited.

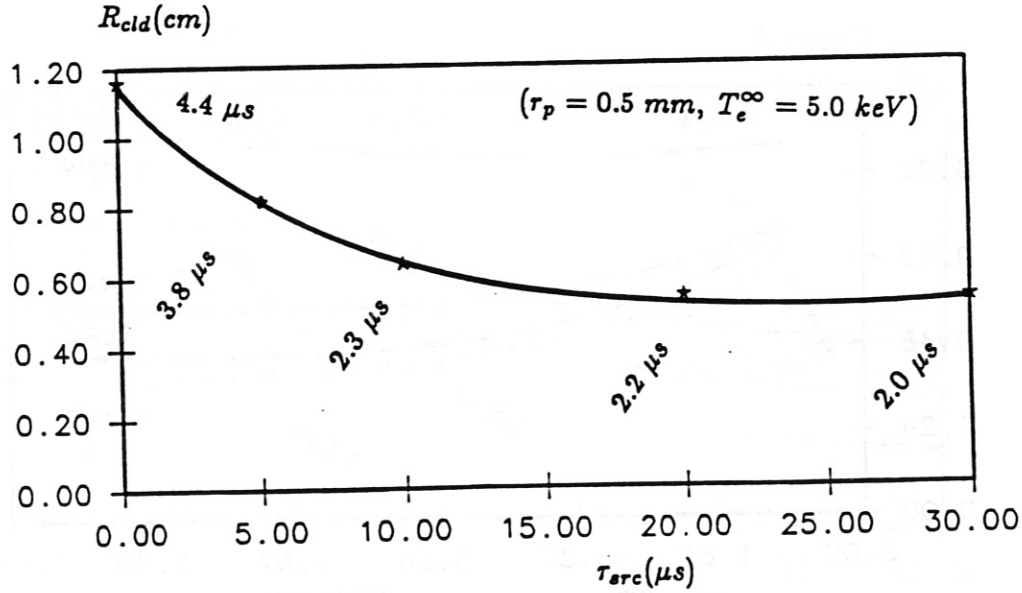

Fig. 19 Effect of the source strength (source duration with ΔN fixed) on the maximum cloud radius ($r_p = 0.5\ mm$, $T_e = 5\ keV$).

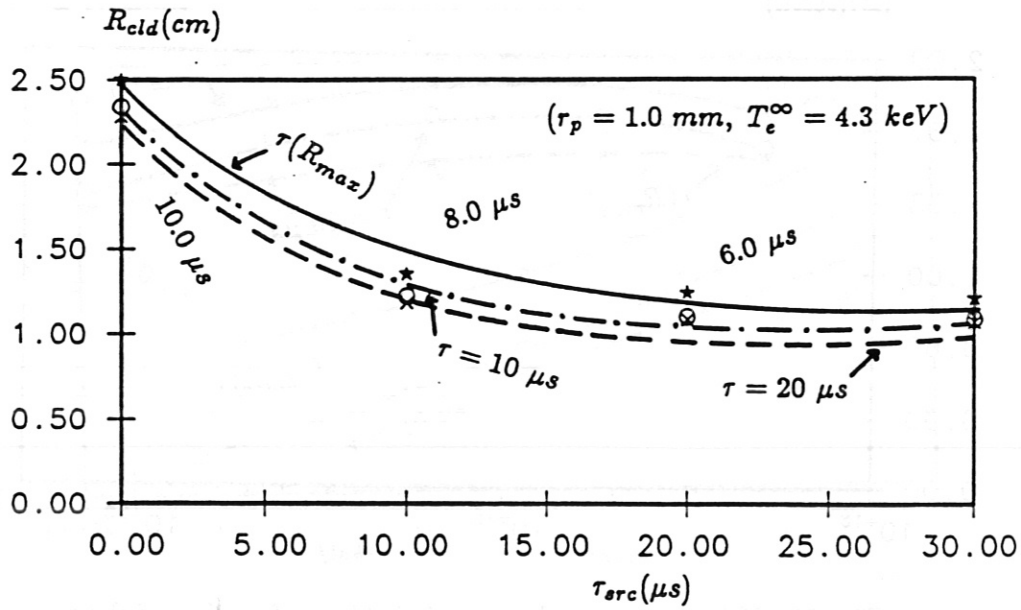

Fig. 20 Effect of the source strength duration on the maximum cloud radius ($r_p = 1\ mm,\ T_e = 4.3\ keV$).

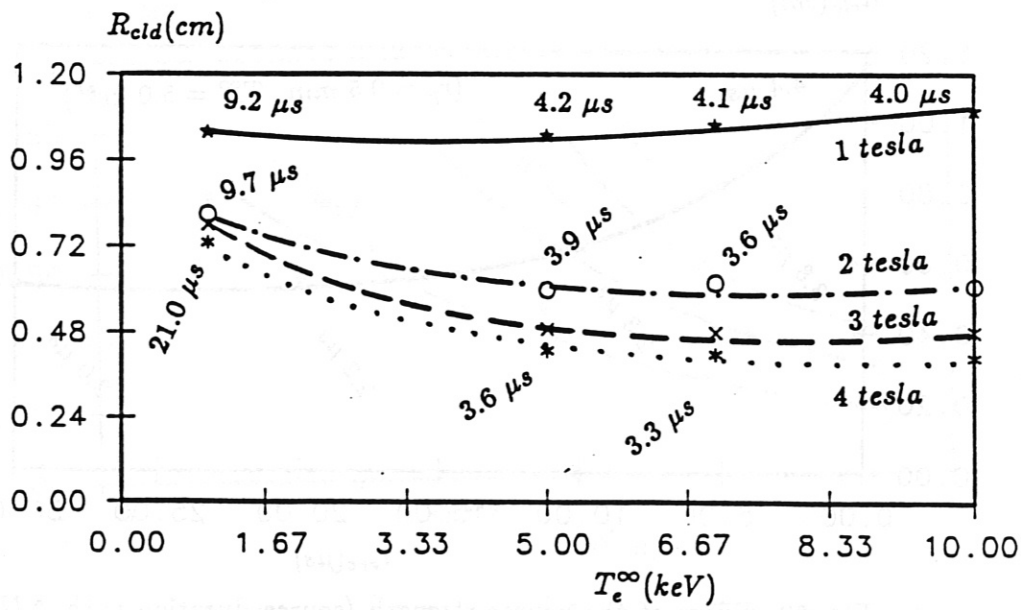

Fig. 21 Maximum cloud radius as a function of plasma temperature for various m.f. strengths (stopping time $\tau_{(R_{max})}$ is also displayed).

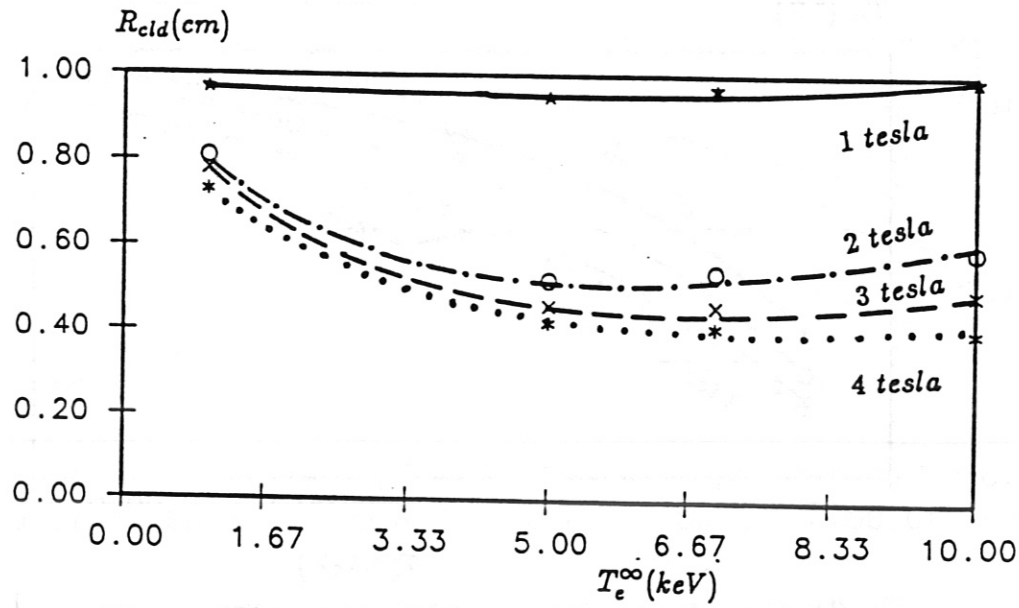

Fig. 22 Cloud radii at expansion time 20 μs as functions of plasma temperature and m.f. strength.

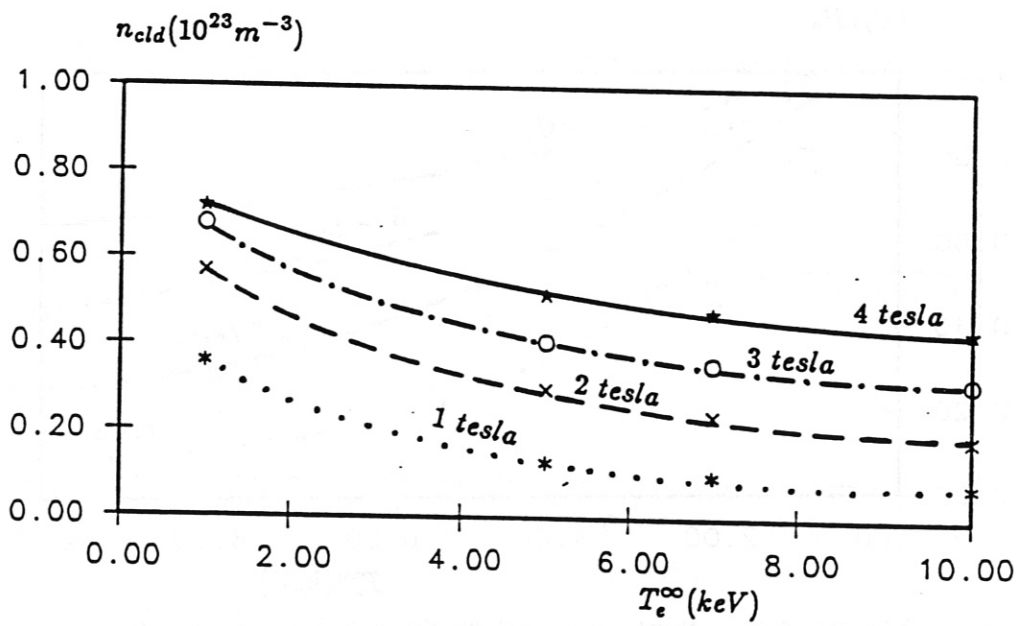

Fig. 23 Cloud density after expansion time 20 μs as function of plasma temperature and m.f. strength.

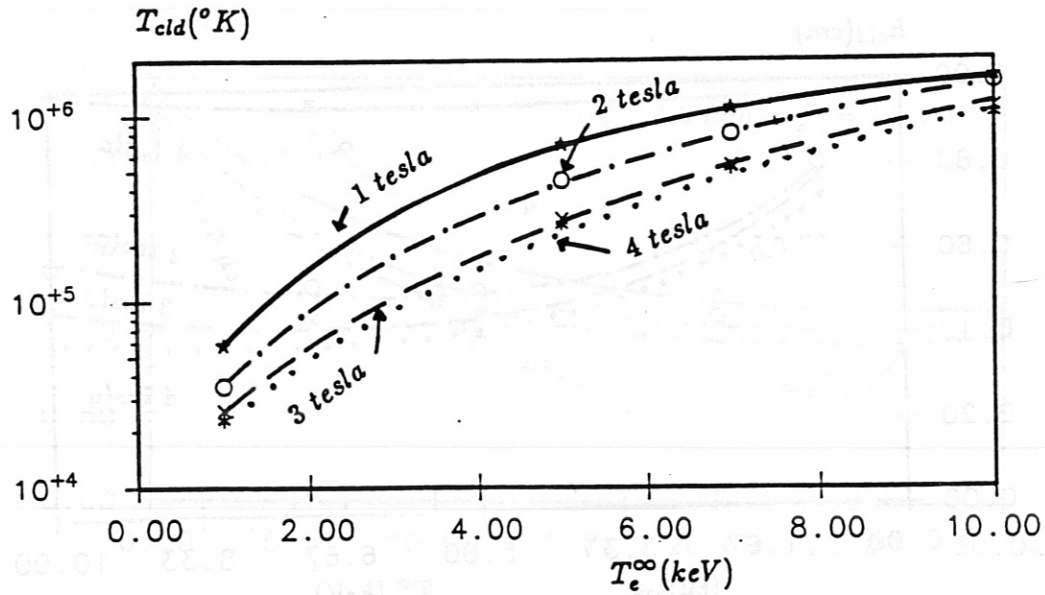

Fig. 24 Cloud temperature at expansion time of 20 μs as a function of plasma temperature and m.f. strength.

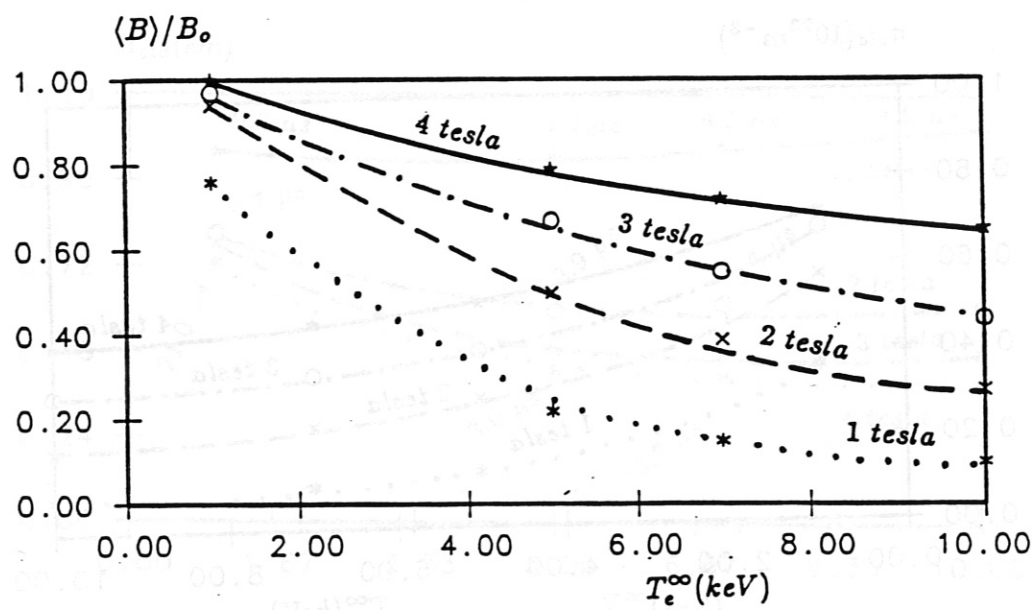

Fig. 25 Diamagnetic state at $\tau = \tau(R_{max})$ as a function of plasma temperature and m.f. strength.

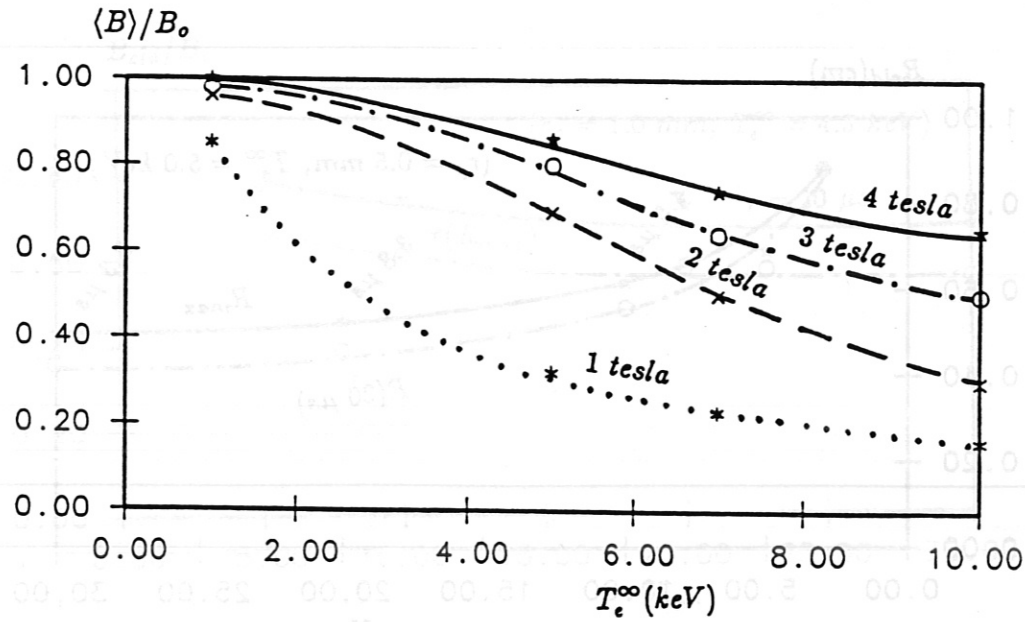

Fig. 26 Diamagnetic state after 20 μs as a function of plasma temperature and m.f. strength.

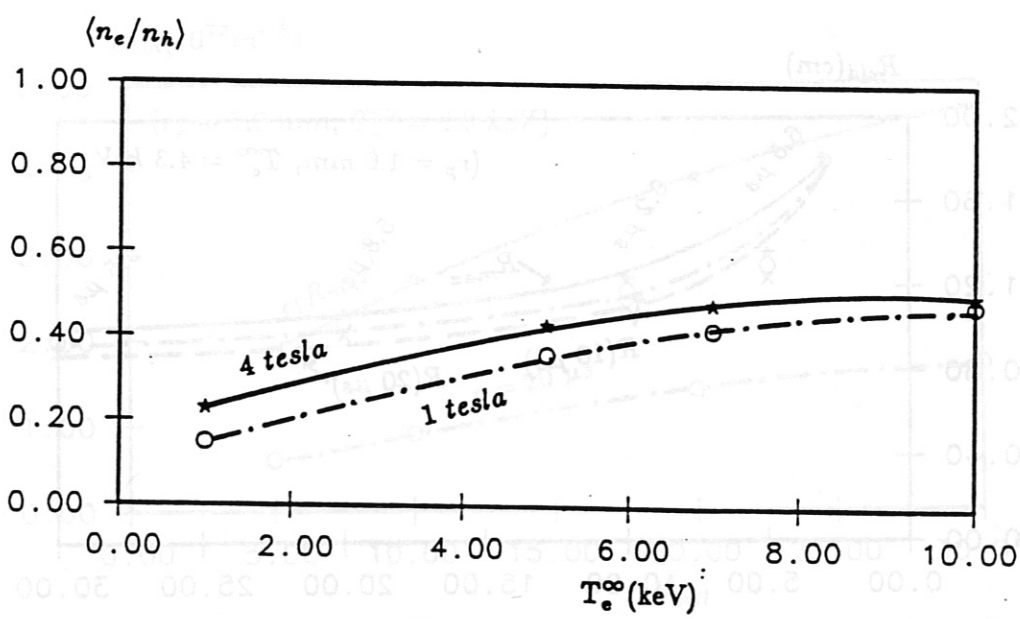

Fig. 27 Bulk ionization degree at $\tau = \tau(R_{max})$ as a function of plasma temperature and m.f. strength.

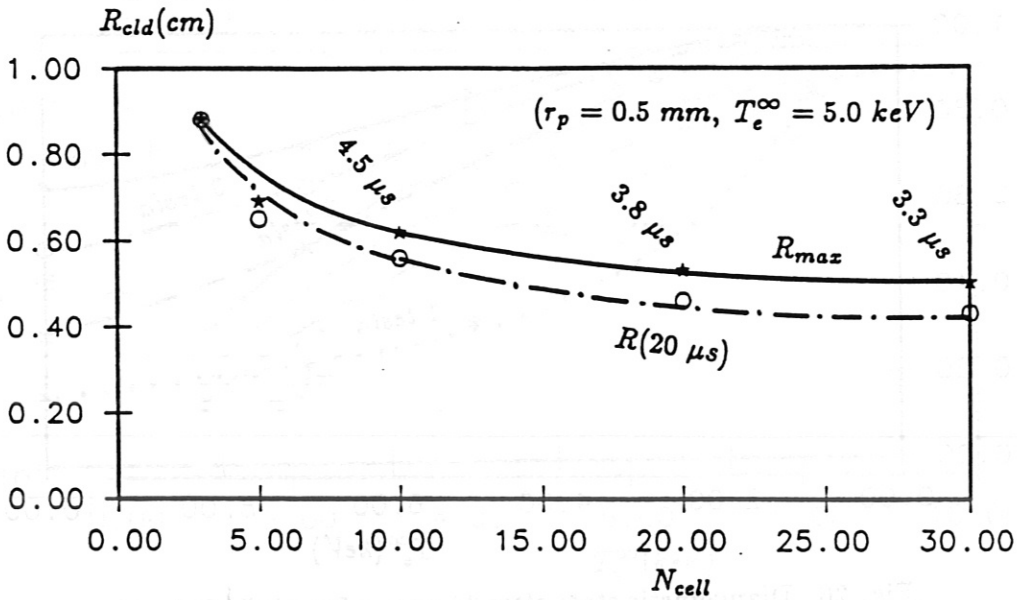

Fig. 28 Effect of the number of Lagrangian cells used on the maximum plasmoid radius.

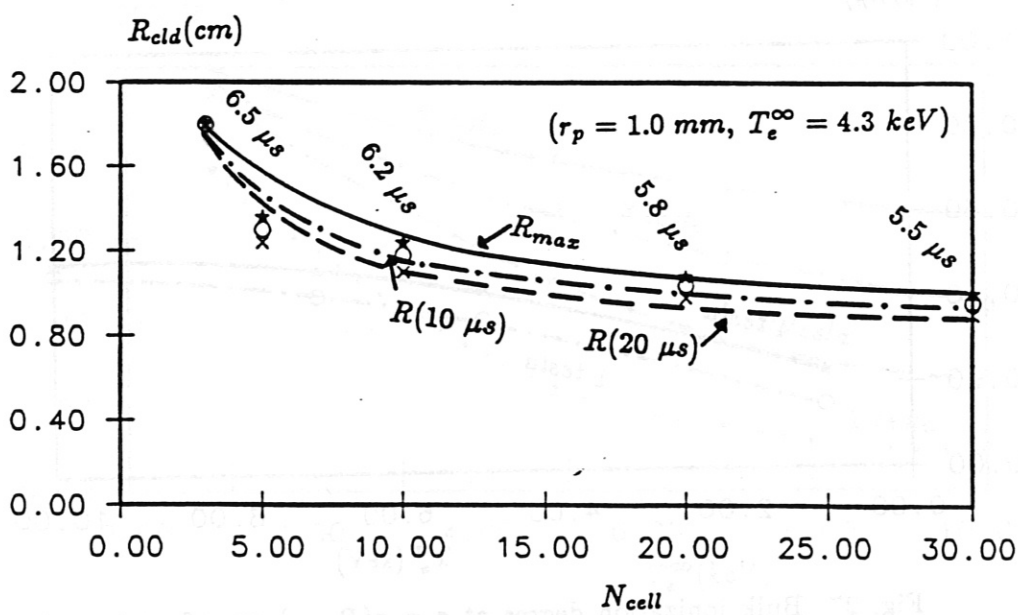

Fig. 29 Effect of the number of Lagrangian cells used on the maximum plasmoid radius.

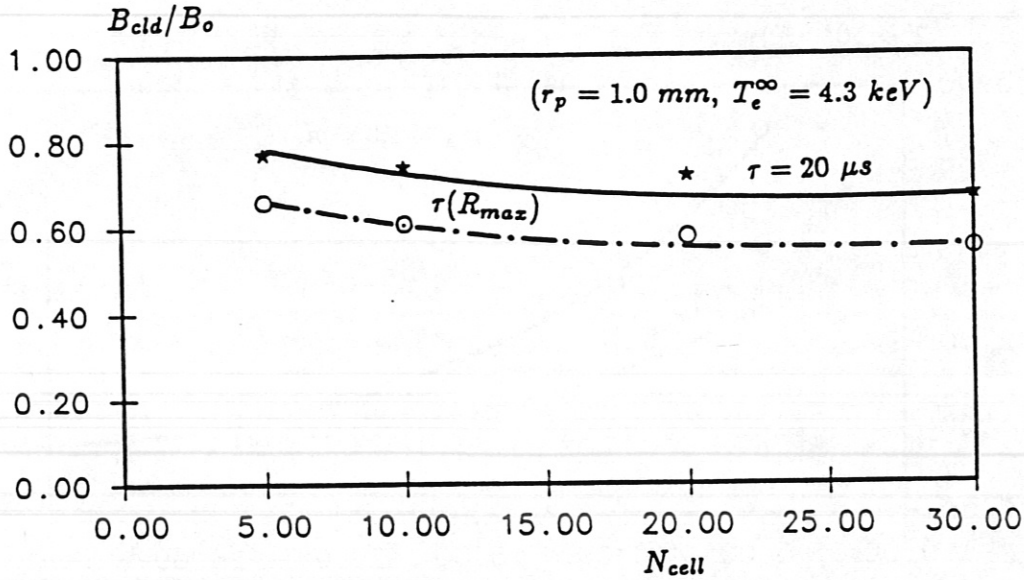

Fig. 30 Diamagnetic state of the plasmoid as a function of the number of Lagrangian cells.

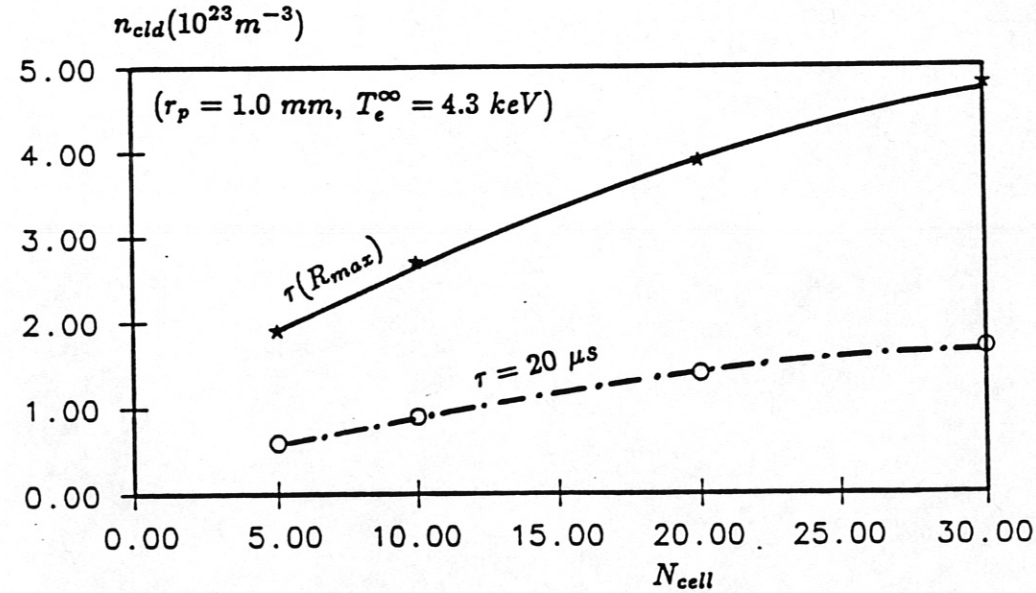

Fig. 31 Effect of the number of Lagrangian cells used on the plasmoid density.

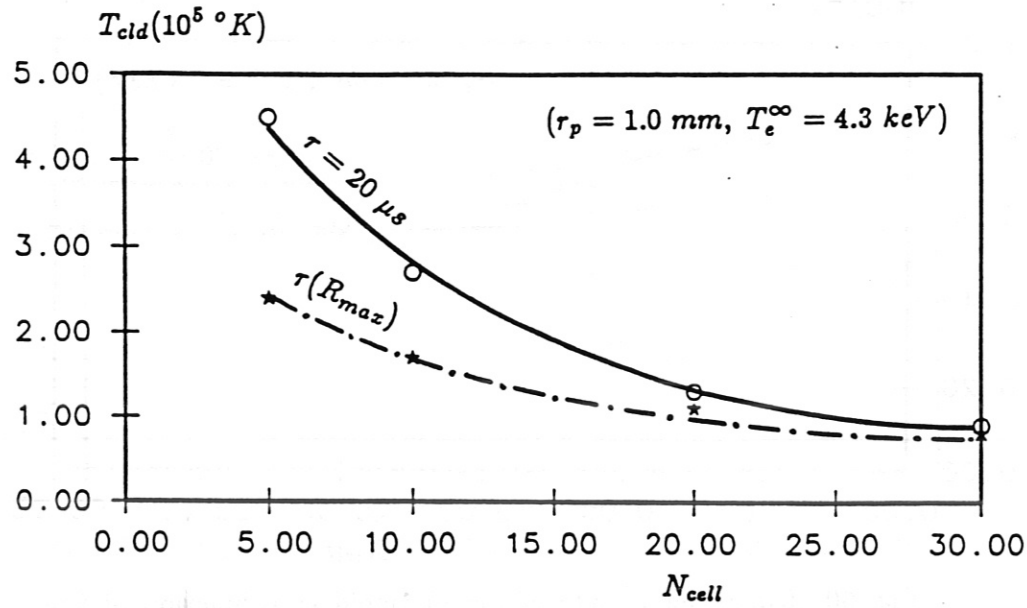

Fig. 32 **Effect of the number of Lagrangian cells used on the plasmoid temperature.**